3.7 Beam Delivery System

3.7.1 Introduction

The Beam Delivery System (BDS) is the transfer line which transports the beam from the linac exit to the interaction point (IP) of the collider. Its main function is to demagnify the beams and to bring them to collisions with spot sizes down to 845 nm $\times$ 19 nm at the center of the detector. The overall 67×167 demagnification from linac to IP is mostly produced by a strongly focusing quadrupole doublet 3 m distant from the IP. Together with a weaker upstream doublet, it composes a final transformer (FT), or telescope, with 15×50 demagnification.

Even with the small 34 μrad $\times$ 27 μrad beam angular divergences at the IP corresponding to the design emittances listed in Table 3.1.2, the chromaticity of this last doublet, which is roughly given by the ratio $\hat{\sigma}_{\rm Q}/\sigma^*$ of the maximum beam size in the last doublet to the beam size at the IP, is too large in comparison with the expected 10^{-3} incoming beam relative energy spread. The FT is therefore preceded by a Chromatic Correction Section (CCS) where sextupoles, located in dispersive regions, create the necessary quadrupole correction for the off-energy particles. The energy bandwidth of this correction determines the energy acceptance of the whole system.

The optics of the Final Focus System (FFS), namely the combination of the Chromatic Correction Section and the Final Transformer, derives from the one of the SLAC Linear Collider FFS [1] with one essential difference consisting in separate, rather than interleaved, horizontal and vertical chromaticity correction sections. The non-interleaved CCS optics which requires more space but in return reduces considerably the amount of non-linear aberrations, has been adopted and operated successfully by the Final Focus Test Beam (FFTB) facility [2] at SLAC.

The transverse beam tails passing through the doublet quadrupoles produce synchrotron radiation which in turn can be a source of background in the detector. The photon energies and angles are maximum in the last doublet where masking is difficult. As seen in Fig.3.7.1, the collimation requirements for a complete clearance of the interaction region is about $14\,\sigma_x \times 46\,\sigma_y$. The beam halo, possibly generated in the linac, is therefore scraped off in the collimation section (CS) by an arrangement of spoilers and absorbers described in Section 3.7.8.

A short Linac Matching Section (LMS) matches the beam from the linac exit to the entrance of the collimation section.

The essential ability to measure the beam emittances after the linac and before final focus system and to correct the incoming transverse coupling is provided by the Tuning and Diagnostic Section (TDS), described in Section 3.7.5, following the Collimation Section.

Finally, changing the beam sizes and angular divergences at the IP in order to optimize the collision parameters without modifying the FT and CCS sensitive optics can be done in the Beta Matching Section (BMS), located between the TDS and the CCS.

After colliding head-on, the spent beams are deflected by an electrostatic separator

at the exit of the detector, and further downstream by septum magnets. In order to maintain a straight orbit for the incoming beam in the separator, a weak magnetic field is superimposed to exactly cancel the electrostatic force acting on the incoming beam while doubling its effect on the outgoing one. After extraction, the positron beam is guided to its dump, and the electron beam is used for positron production.

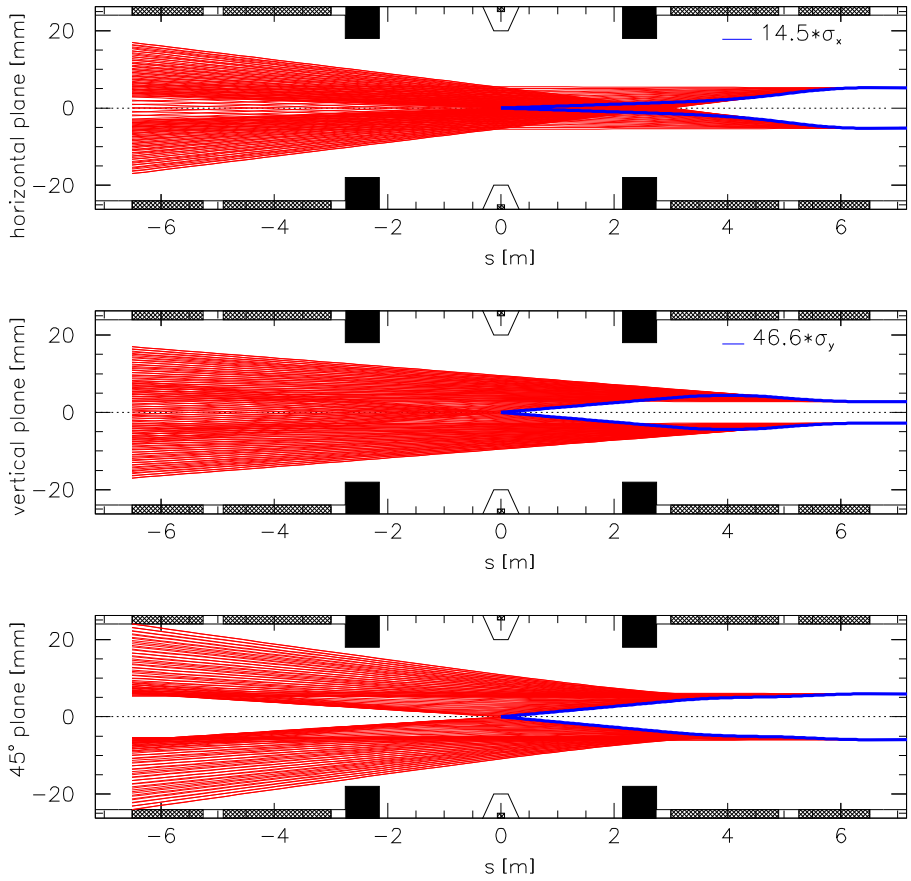

Figure 3.7.1: *Synchrotron Radiation emitted in the last doublet quadrupoles through the vertex detector and opposing doublet apertures.*

3.7.2 Magnet Lattice and Optics

The magnet layout and beam sizes along the beam delivery system are shown in Fig.3.7.2. The BDS is composed of the 6 sections whose function has been described above. These sections, listed in Table 3.7.1 with some of their characteristics, are described thereafter.

• The **Linac Matching Section** (LMS) is composed of six quadrupoles, following the last focusing linac quadrupole, which provide enough free parameters to match the

	L [m]	s [m]	β_x [m]	β_y [m]
Linac Matching Section (LMS)	17.3	0.0	113.445	19.489
Collimation Section (CS)	389.5	17.3	13.081	7.244
Tuning and Diagn. Section (TDS)	182.2	406.8	13.081	7.244
Beta Matching Section (BMS)	31.5	589.1	21.383	9.655
Chromatic Corr. Section (CCS)	331.4	620.6	5.614	1.767
Final Transformer (FT)	142.5	951.9	5.614	1.767
Interaction Point (IP)		1094.4	0.025	0.0007

Table 3.7.1: *Orbit lengths and beta functions at the entrance of the BDS sub-sections. The overall x and y demagnification factors are* 67×167.

beam to the entrance of the collimation section and therefore to tune the beam sizes at the collimator locations.

• The **Collimation Section** (CS) provides 4 regions of combined high horizontal and vertical betas as well as large horizontal dispersion. Each region hosts a pair of Titanium collimators to intercept off-momentum and large (x and y) amplitude particles. In normal operation, their aperture is set to $8\,\sigma_x$ and $32\,\sigma_y$ and they collimate particles with more than 2% momentum offset. The last two collimator pairs are in phase with the last doublet: they intercept the sine-like trajectories (with respect to the IP) which have the largest amplitudes in this doublet and therefore produce the most harmful part of the synchrotron radiation in the last quadrupoles. The two upstream collimator pairs are in phase with the IP and thus intercept the cosine-like trajectories. This second phase collimation is necessary to protect the detector from phase mixing, of chromatic or non-linear origin, occurring between the collimation section and the last doublet. To minimize the chromatic phase mixing in the CS itself, the chromaticity created by the CS high-beta regions is corrected locally by embedded sextupoles pairs, in a way similar to the one described below for the CCS.

• The **Tuning and Diagnostic Section** (TDS) is a section devoted to measuring and correcting the sensitive transverse coupling, inherited from the Linac transport and/or created in the Collimation Section. The coupling correction is performed in the Skew Quadrupole Correction Section which hosts four skew quadrupoles located at the proper relative phase advances to cancel the four coupling coefficients of the transverse beam matrix. Tuning is done by minimizing the vertical emittance which is measured, together with the horizontal one, in the Emittance Measurement Section (EMS). The EMS is a simple FODO lattice with three and a half 45° cells along which four wire scanners are regularly disposed every 45° in phase space. Each wire scanner measures the horizontal and vertical spot sizes, expected to be about equal to $17\,\mu$m and $3.3\,\mu$m. This is therefore in the range of solid carbon wires as the ones currently and reliably operated in the SLC. The regularity of the beam phase advances and spot sizes at the wire locations optimizes the reconstruction of the transverse emittances from the spot size measurements.

• the **Beta Matching Section** (BMS) contains 7 quadrupoles which allow to

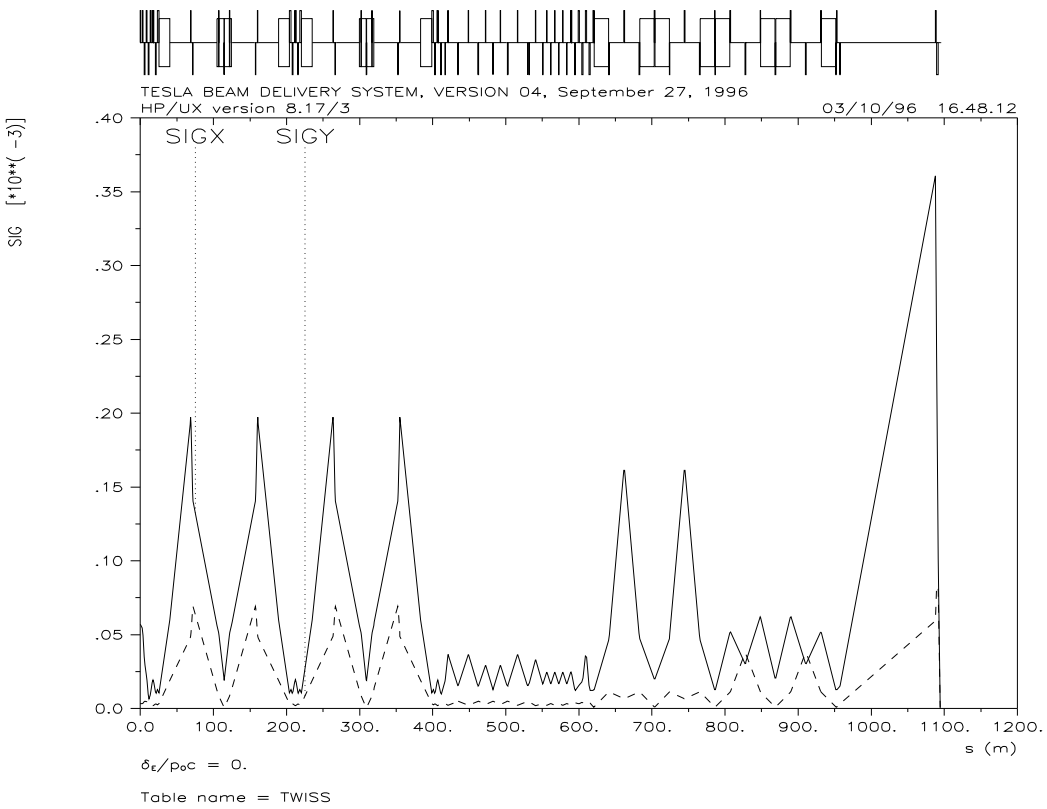

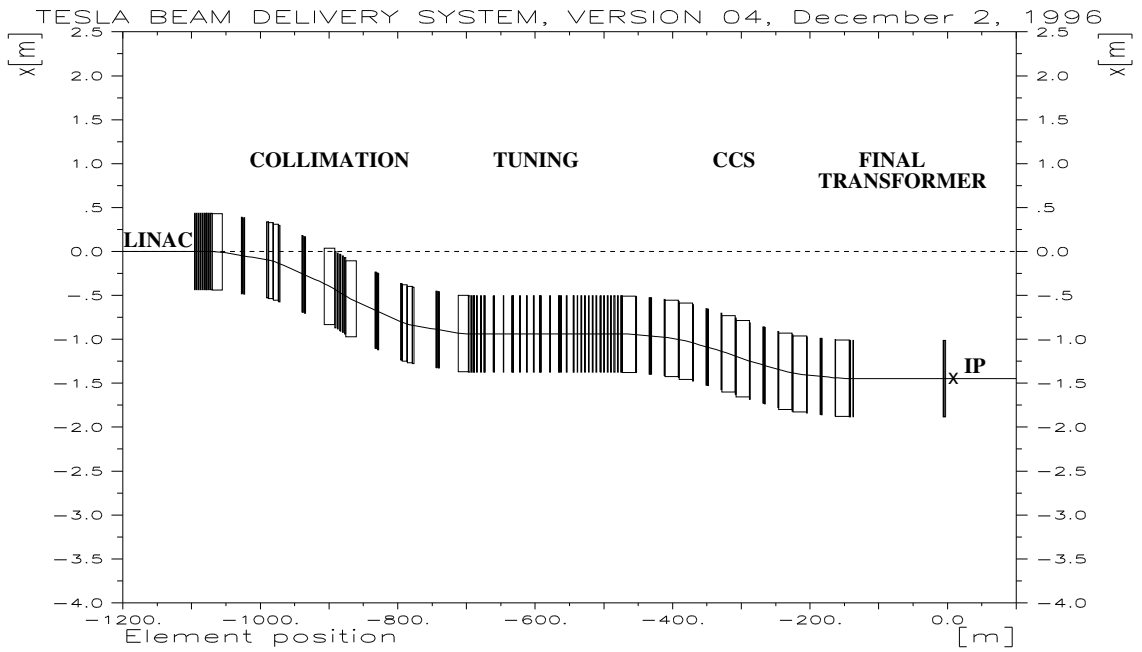

Figure 3.7.2: *Magnet layout and beam spot size (in meters) in the BDS (top), and horizontal survey of the BDS (bottom).*

match the beam matrix at the entrance of the final focus system over a wide range of parameters. Since the final focus system is a pure demagnifying telescopic system, the BMS can therefore be used to fine tune the beam at the IP as well as the phase advance from the collimators to the last doublet. It can also be used, for the start-up operation, to blow up the beam by as much as a factor 10 with a relative variation of the quadrupole gradients limited to about $\pm 20\%$. The BMS magnets need therefore to be tunable over this range.

• The **Chromatic Correction Section** (CCS) is a one-to-one transformer composed of two FODO sections with four 90° cells each. Both sections contain four bending magnets symmetrically disposed to generate a closed horizontal dispersion bump, and a pair of sextupoles to tune the chromaticity. Since the two sections have opposite quadrupole polarities, the first one corrects the horizontal chromaticity and the second one the vertical chromaticity. Each of the four sextupoles is located next to the central quadrupole where the phase advance is a multiple of $\pi/2$ and the relevant beta-function is maximum. In this way the sextupoles do not generate geometric or chromatic aberrations other than the ones needed to cancel the chromatic aberrations from the last doublet. The bandwidth of this system, shown in Fig.3.7.3 is more than sufficient to accept the foreseen 0.1 % bunch energy spread and bunch to bunch energy deviations. With opposite dipole polarities, the two sections create an S-shaped CCS orbit with two opposing deflection angles of about 3 mrad generated by four 19.7 m long dipoles with a field of 32 mT. The beam relative energy spread due to synchrotron radiation along these 8 dipoles and the relative energy loss between sextupoles of the same pair are both very small, lower then 2×10^{-5}.

• The **Final Transformer** (FT) is a telescopic system which achieves the final demagnification of the beam spot sizes by 15 horizontally and 50 vertically. It is composed of a weak and a strong doublet separated by 130 m. The strong final doublet, located inside of the detector, is composed two 2 K superconducting quadrupoles of 250 T/m gradient, 48 mm physical aperture diameter and 1.9 m and 1.25 m lengths, as shown in Fig.3.7.1. Their design is based on successfully tested prototypes for the LHC lattice quadrupoles [3]. Their cross- section is shown in Fig.3.7.4. The two opposing final doublets are separated by 6 m around the IP and their apertures provide enough clearance for the spent beam to allow collisions with zero crossing angle.

• **Spent Beam Extraction**

Because of the 700 ns (about 200 m) bunch separation, the beams can collide head-on and be separated outside of detector in the long drift space between the two doublets of the FT. This is done by a 20 m long electrostatic separator with a field of 4.8 MV/m starting about 10 m after the IP. To prevent synchrotron radiation from hitting the detector, a weak 16 mT magnetic field is superimposed so that the incoming trajectory is not bent. With an overall angular deflection of 0.77 mrad, the outgoing beams are offset by 3 cm from the main beam axis at 60 m from the IP. This separation is large enough for septum magnets to further extract the electron beam towards the positron production system and the positron beam towards its dump.

• **Tracking Results**

Results of tracking simulations through the entire BDS are shown in Fig.3.7.5. They

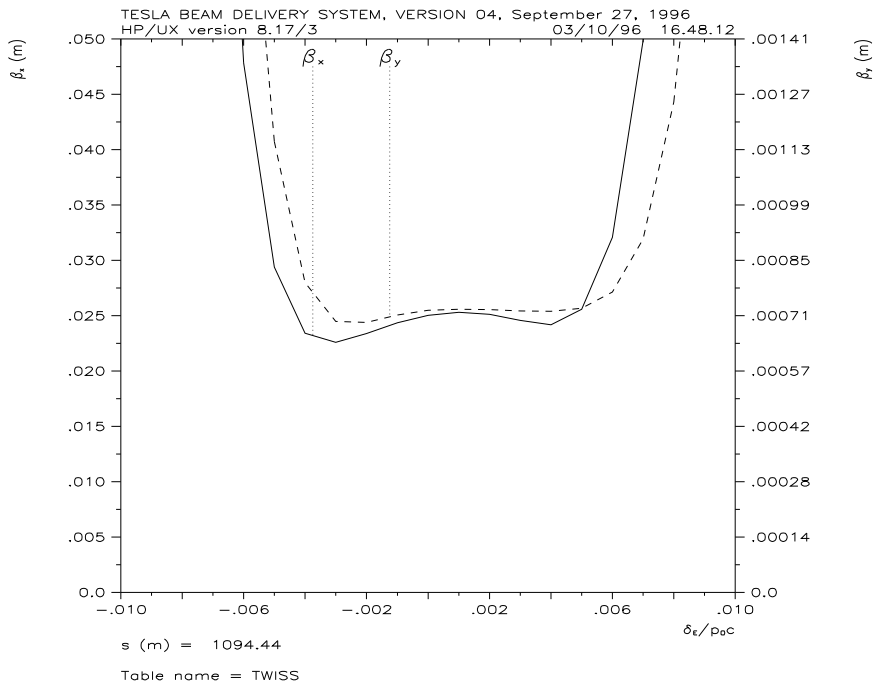

Figure 3.7.3: *Energy bandwidth of the 500 GeV beam delivery system calculated from the energy dependence of the beta-functions at the IP.*

have been performed with MAD [4] and they include the effect of synchrotron radiation in the magnets. Luminosities are calculated from the beam distributions without pinch effect. Up to 2.5×10^{-3} relative energy spread the effect of non-linear aberrations on the beam IP spot sizes is negligible and the expected luminosity is 97 % of the design one.

• **Magnets and Beam Pipe Apertures**

The required aperture radii of the BDS quadrupoles (final doublet excepted) and sextupoles are shown in Fig.3.7.6 for a 1 T pole-tip field which is an achievable field for room temperature magnets. With this assumption the tightest apertures are about 5 mm radius. A 1 cm diameter stainless steel beam pipe is acceptable from the impedance point of view since the relative energy spread and energy loss induced by the resistive wakefields along 1.1 km of beam pipe are about 3×10^{-5}. It also provides a sufficiently large linear acceptance of about 25 horizontal and 100 vertical standard deviations. In principle, a larger aperture is possible by increasing the length of some of the magnets.

• **The 800 GeV Upgrade**

The 500 GeV cm-energy Beam Delivery System optics described above can be

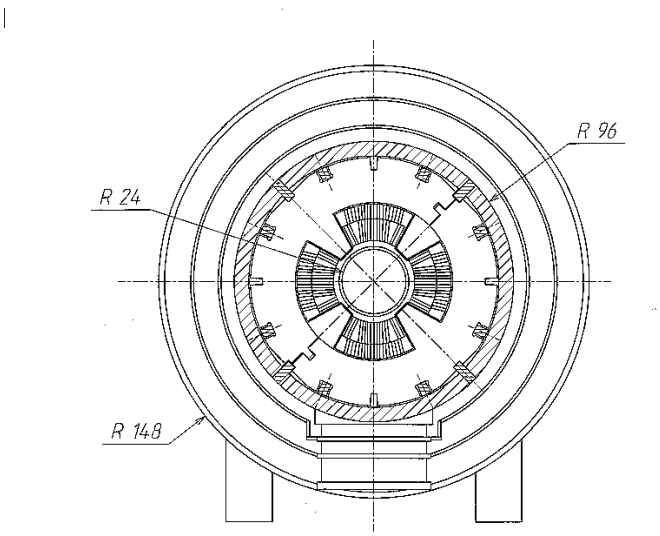

Figure 3.7.4: *Last doublet superconducting quadrupole cross-section.*

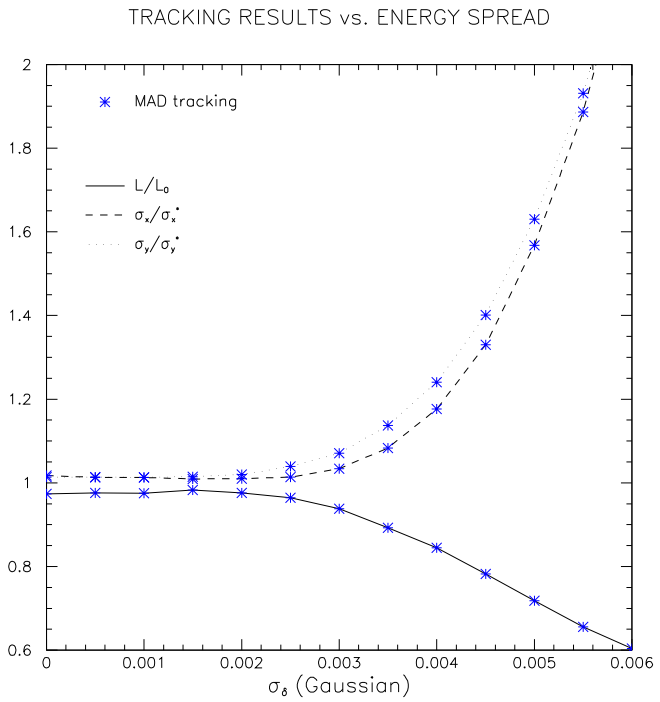

Figure 3.7.5: *Dependence of the spot sizes and luminosity, normalized to their design values, on the Gaussian RMS relative energy spread.*

adapted to 800 GeV cm-energy with the same magnets, except for the last doublet quadrupoles. Since the beta-functions at the IP are identical to the ones for 500 GeV cm-energy, the Twiss parameters over the BDS are kept essentially unchanged by in-

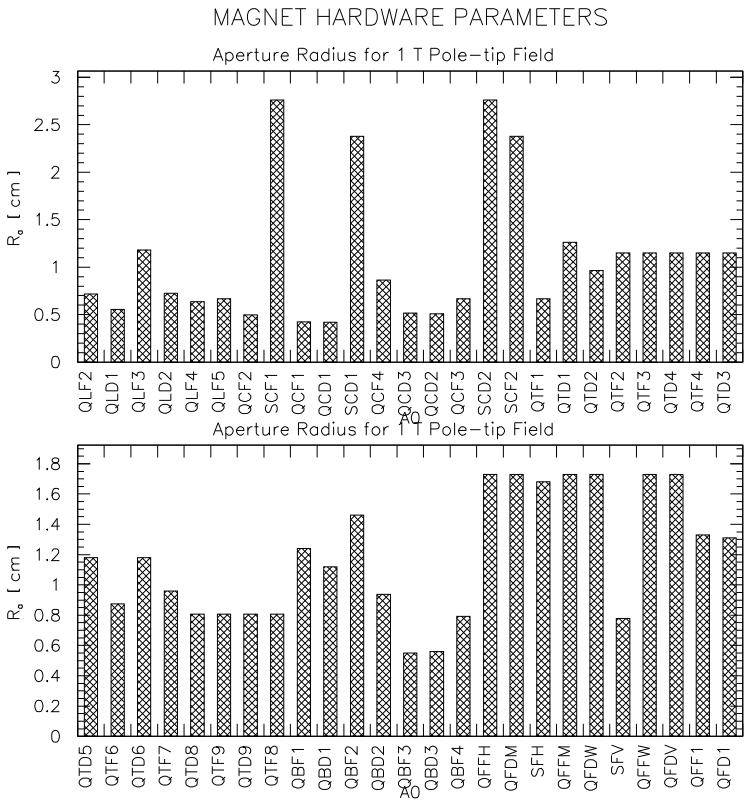

Figure 3.7.6: *Aperture radii of the BDS magnets (dipoles and the final SC quadrupoles excepted) assuming 1 T pole tip field.*

creasing the BDS quadrupole focusing strengths in proportion to the beam energy. However, in order not to increase the gradient of the last doublet superconducting quadrupoles, while keeping a 3 m drift space to the IP, the FT is re-designed with longer, namely 2.71 m and 1.67 m long, SC magnets. The FT demagnification is also reduced to 15×30 to keep the upstream doublet at the same location. This reduction is exactly compensated by increasing the demagnification of the Beta Matching System with some retuning of the BMS quadrupoles. The resulting energy bandwith of the system is shown in Fig.3.7.7. The strengths of the dipole magnets in the entire system are sufficiently low to keep emittance growth from synchrotron radiation at a level of a few percent.

Spent beam separation is achieved by lengthening the electrostatic separator to 32 m which gives 2.6 cm outgoing beam offset in the septum magnets.

3.7.3 Sensitivity to Errors

Displacement and magnet errors occuring upstream of the beta matching section (BMS) will be accurately detected in the diagnostic section and corrected. Downstream errors

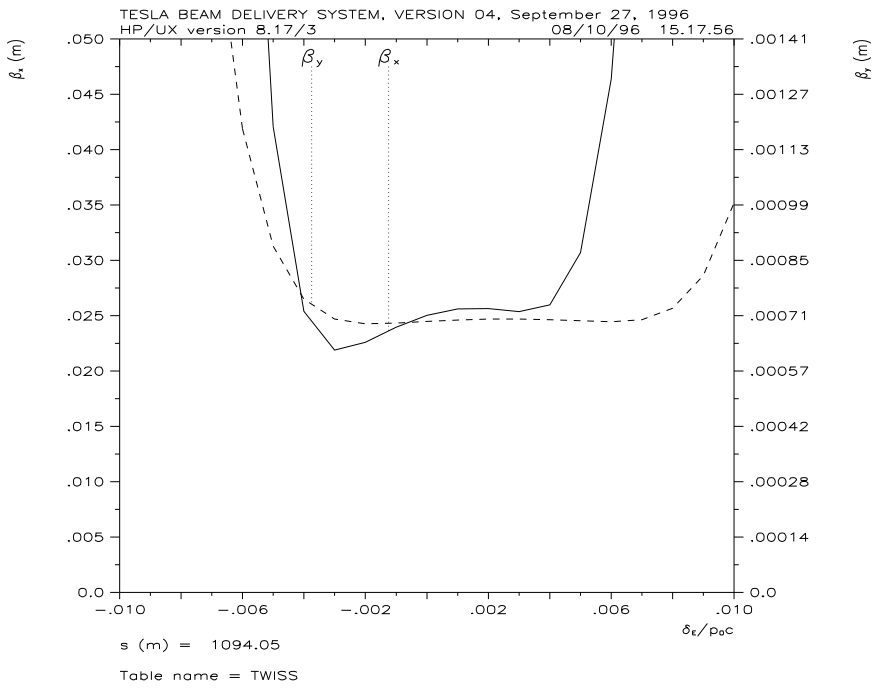

Figure 3.7.7: *Energy bandwidth of the 800 GeV beam delivery system calculated from the energy dependence of the beta-functions at the IP.*

will be more difficult to measure with the fewer and less precise beam size monitors equiping the IP and its image point at the exit of the CCS. This section is thus devoted to the study of the sensitivity to errors of the BMS and FFS final sections.

This error sensitivity is calculated from the first and second order derivatives of the IP orbit and transfer matrix with respect to magnet errors as well as from the first order derivatives of the T-matrix of the transfer map. This information, stored in large arrays, allows one to calculate the sensitivity of the optical system to any kind of misalignments, vibrations or magnet field instabilities.

Once translated in terms of luminosity loss and spot size growth, this information can also be used to calculate tolerances of the final focus system to misalignment or field errors. To do so, one has to specify a model that describes the source of these errors, their spectrum and correlations over time and distance. In this section, the following two simple situations are considered: first, fixed (or static) errors affecting only one magnet, assuming all other elements are perfectly aligned and tuned, and second, uncorrelated random transverse vibrations affecting all magnets of both final focus beam lines. More realistic models taking into account ground motion are studied in Sect.3.7.4.

• **Static Tolerances**

The static tolerances are shown in Figs. 3.7.8 and 3.7.9 assuming a beam energy spread of 0.1 %. They are derived from a 2% reduction of the luminosity calculated by assuming that one beam is perfectly matched while the other beam is affected by the error considered. In all pictures, the inverse tolerances are plotted in such a way that the highest bars correspond to the tightest tolerances. Black bars give the tolerances with no steering corrections, while the white bars give tolerances with IP offset corrections included. Besides the last doublet quadrupoles which, as expected, set the tightest tolerances, the CCS bending magnets show also a high sensitivity to skew rotations and field errors. Dispersion errors, especially vertical ones, are mainly due to the last CCS quadrupoles and the first FT doublet.

• **Uncorrelated Vibration Tolerances**

For the model of mechanical vibrations where magnet transverse motions are uncorrelated and have the same horizontal and vertical RMS, $\sigma_x^{(mag)}$ and $\sigma_y^{(mag)}$, the RMS of the resulting relative beam offset, crossing-angle and the single beam dispersions at the IP are then given by:

$$\begin{array}{ccc} \sigma_{\delta x^*} = 0.88 \times \sigma_x^{(mag)} & , & \sigma_{\delta y^*} = 0.24 \times \sigma_y^{(mag)} \\ \sigma_{\theta_x^*} = 8.95\,\mathrm{rd}/m \times \sigma_x^{(mag)} & , & \sigma_{\theta_y^*} = 44.7\,\mathrm{rd}/m \times \sigma_y^{(mag)} \\ \sigma_{D_x^*} = 98.8 \times \sigma_x^{(mag)} & , & \sigma_{D_y^*} = 19.2 \times \sigma_y^{(mag)} \end{array}$$

Actually the offset RMS $\sigma_{\delta x^*}$ and $\sigma_{\delta y^*}$ do not include the dominant contribution from both the opposing last doublets which can be directly read from Figs. 3.7.8 and 3.7.9.

In this model, small luminosity losses can be parametrized as

$$\delta\mathcal{L}/\mathcal{L}_0 = -2\% \times \{(\sigma_x^{(mag)}/318\,\mathrm{nm})^2 + (\sigma_y^{(mag)}/35.2\,\mathrm{nm})^2\} \quad \text{(no offset correction)}$$

for the fast jitter with no steering correction done (again excluding the contribution from the last doublets), and

$$\delta\mathcal{L}/\mathcal{L}_0 = -2\% \times \{(\sigma_x^{(mag)}/558\,\mathrm{nm})^2 + (\sigma_y^{(mag)}/204\,\mathrm{nm})^2\} \quad \text{(with offset correction)}$$

for the case where steering correction is done. In the first case, the luminosity loss is dominated by the beam relative offsets. In the second case, this contribution is removed and the luminosity loss is mainly coming from spot-size growth with a small contribution from the vertical crossing angle. Since a fast IP orbit steering feedback is foreseen, the latter case is the relevant one here. The 2 % luminosity loss tolerances can be read immediately from the above expressions. With the 0.1 % energy spread considered, the horizontal spot-size growth induced by horizontal misalignments comes 36% from waist-shift and 64% from horizontal dispersion while the vertical spot-size growth induced by vertical misalignments comes half from yx'-coupling and half from vertical dispersion. The vertical spot-size growth induced by horizontal misaligments comes totally from waist-shift, and the horizontal spot-size growth induced by vertical misalignments comes totally from xy'-coupling.

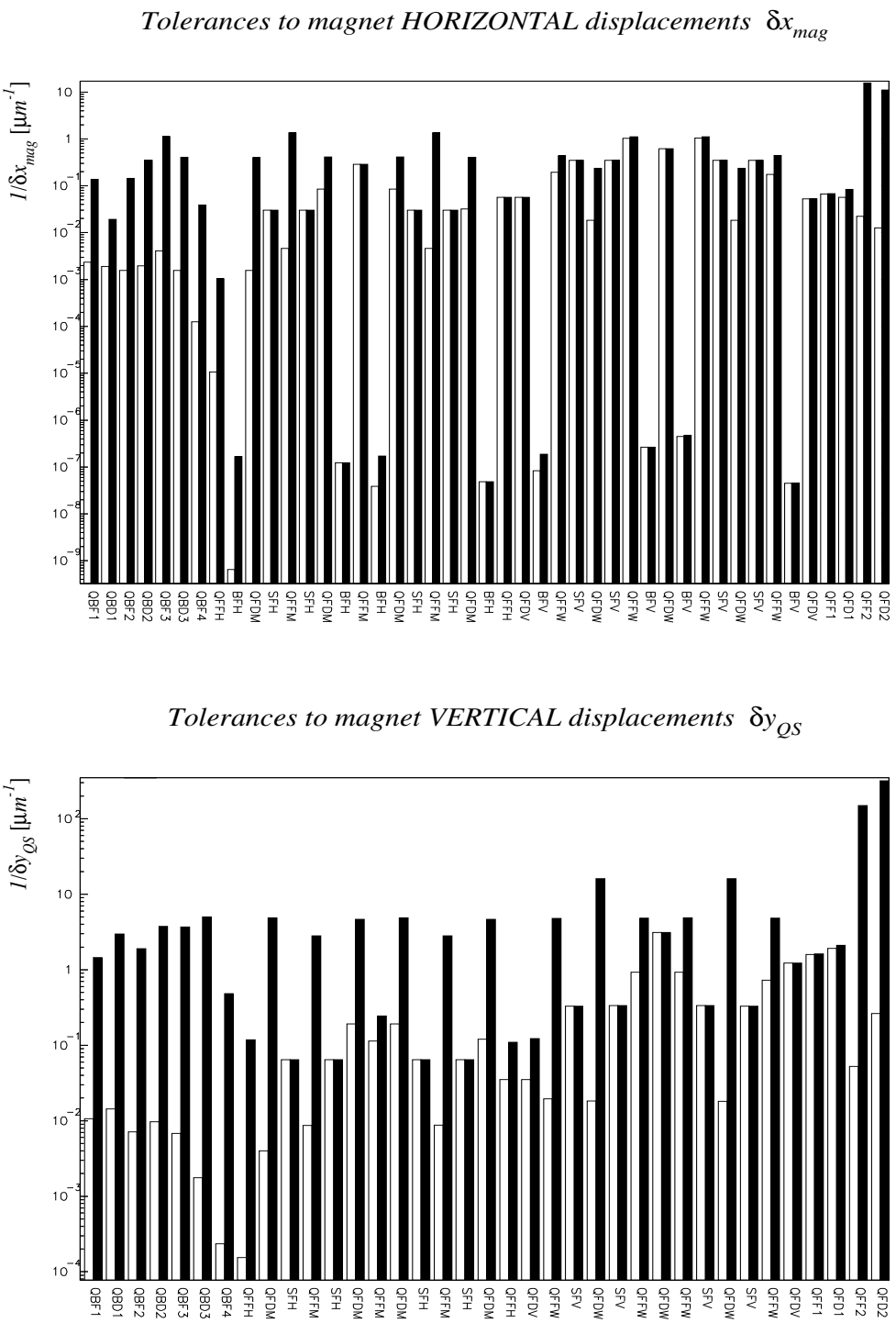

Figure 3.7.8: *FFS Sensitivity to transverse displacements (black bars: with IP offset ; white bars: IP offset corrected).*

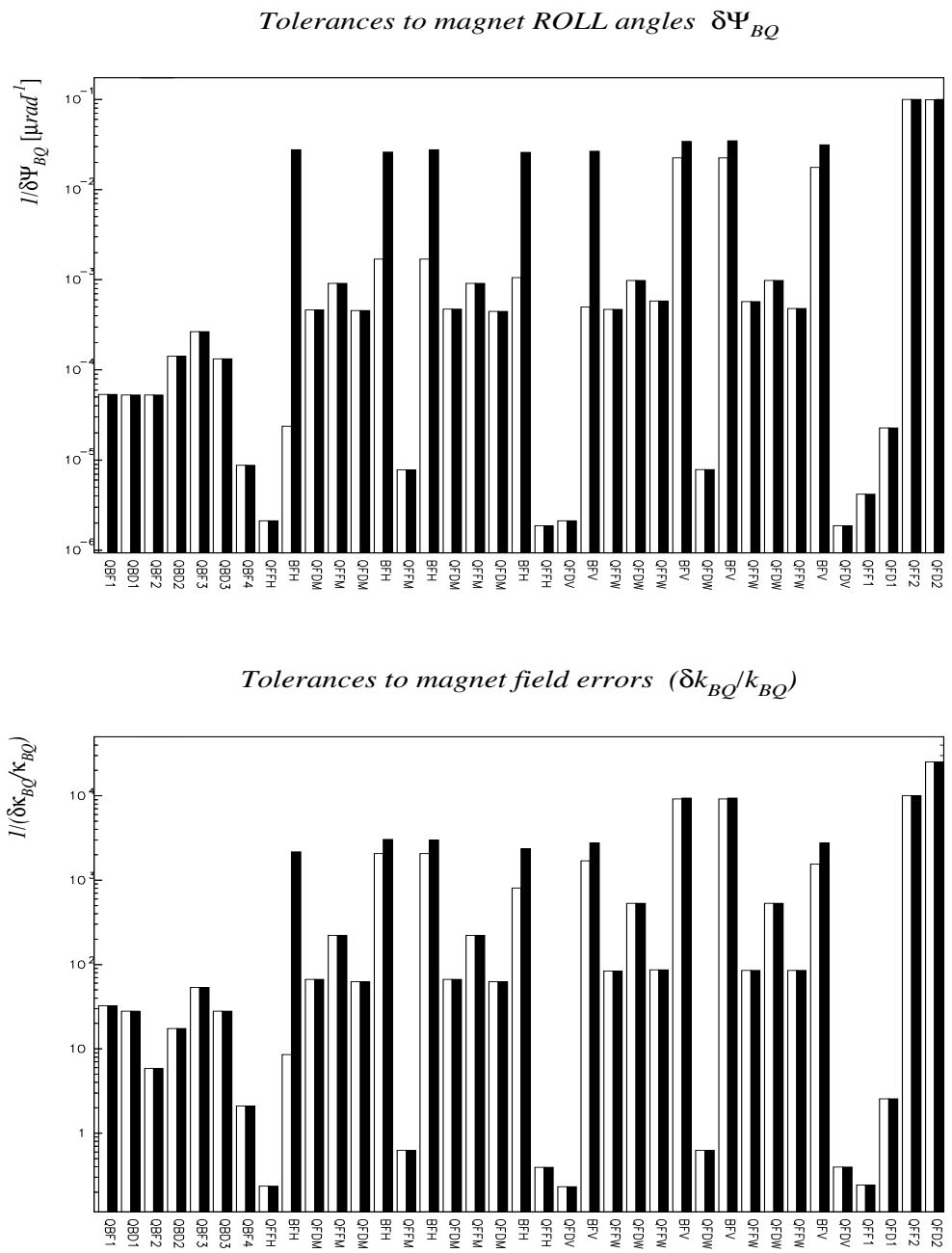

Figure 3.7.9: *FFS Sensitivity to skew rotations and field errors (black bars: with IP offset ; white bars: IP offset corrected).*

3.7.4 Ground Motion

Ground motion is an important issue for the linear collider, because it may result in misalignment of focusing and accelerating elements and thus in trajectory offset and emittance dilution. Ground motion influence is more severe in the beam delivery system, where tolerances are the tightest. It is therefore natural to discuss it in detail in this chapter. Some relevant considerations appear in the chapter describing beam dynamics in the main linac as well.

• **Mathematical description of ground motion** consists in spectral representation, because the relevant quantity $y(t,s)$, the vertical position of the ground surface, can be considered to move in a "random" fashion and should be characterized therefore by the corresponding power spectrum $P(\omega,k)$ [11]. Other characteristics (such as the measurable temporal power spectrum of absolute motion taken in a single point $p(\omega)$, the spectrum of relative motion of two separated points $\rho(\omega,L)$, the correlation $C(\omega,L)$ and the power spectrum $P(t,k)$ of the misalignment $y(t,s)-y(0,s)$ etc...) are all related to $P(\omega,k)$.

While spectral properties of the ground motion are described by the power spectrum, spatial spectral properties of the considered focusing structure of the linear collider can be described by a spectral response function [11]. The errors induced by misalignments, such as the rms beam offset or the rms beam dispersion at IP, can be determined by the integral of the corresponding spectral response function with the power spectrum of the misalignment. For example the rms beam dispersion at the IP is

$$\langle \eta^2(t) \rangle = \int_{-\infty}^{\infty} P(t,k)\, G_\eta(k)\, \frac{dk}{2\pi}$$

The spectral response functions $G_{\rm off}(k)$ or $G_\eta(k)$ show, in terms of rms relative offset or beam dispersion, the spectral response of the considered focusing section to the misalignment having spatial period $2\pi/k$ (Fig.3.7.10).

The spectrum of misalignments, if produced by ground motion, exhibits the following evolution

$$P(t,k) = \int_{-\infty}^{\infty} P(\omega,k)\ \ 2\,[1-\cos(\omega t)]\, \frac{d\omega}{2\pi}$$

In most cases it is essential to have the orbit stabilization feedback taken into account. The equilibrium beam characteristics, for example the rms equilibrium beam offset at the IP, can then be estimated using the function $F(\omega)$, which characterizes the spectral performance of the feedback, convoluted with the ground motion spectrum and the corresponding spectral response function.

However, orbit stabilization or tuning algorithms may be quite complex and their performance may depend on many factors such as BPM or mover resolution etc... In these cases analytical methods based on the spectral response function cannot be applied, thus direct simulations of ground motion [17] and particle tracking should be used to determine the beam degradation.

• **Measured information on ground motion** is available from studies performed in many laboratories all over the world [5]-[10].

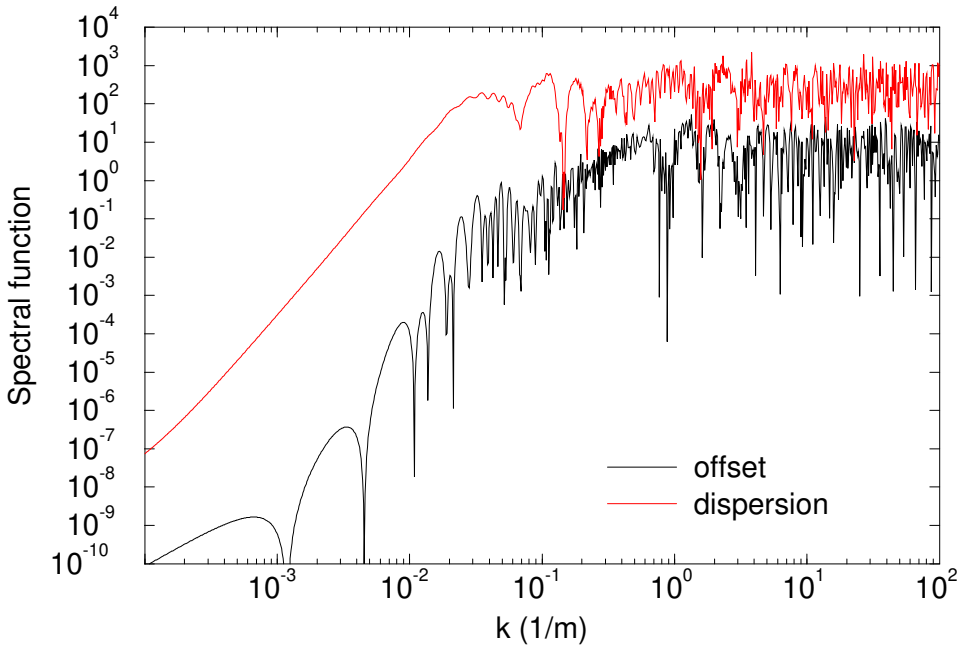

Figure 3.7.10: *Spectral response functions for the relative offset $G_{\rm off}(k)$ and for the beam dispersion $G_\eta(k)$ for the TESLA Beam Delivery system.*

It is known that the power spectrum $p(\omega)$ of absolute ground motion (which contains contribution of all k) grows very fast with decreasing frequency. In quiet conditions it behaves approximately as $p(\omega) \propto 1/\omega^4$ in a wide frequency band. The motion is unavoidable as it consists of seismic activity. At low frequency $f < 1$ Hz significant contributions to absolute ground motion come from remote sources like water motion in the oceans, atmospheric activity, temperature variations etc... A well-known example of the ocean influence is the peak in the band 0.1 – 0.2 Hz with a few micrometers amplitude (Fig.3.7.11).

On the other side, in the band $f > 1$ Hz the human produced noise is usually dominating over the natural noise and the power spectrum depends very much on the local conditions (location of sources, depth of tunnel etc.). Locally generated noise can be much bigger than remotely generated. For example the spectrum measured at the tunnel of an operating circular accelerator (DESY HERA collider) presents high amplitudes at $f > 1$ Hz due to noise generated by different technical devices (Fig.3.7.11). This noise may have a big amplitude and poor spatial correlation. Technical devices of the future linear collider therefore should be properly designed in order to pass as low vibration as possible to the tunnel floor.

It is known from correlation measurements [6, 10] that in quiet conditions the motion in the band $f > 0.1$ Hz can be considered as wave-like, i.e. the frequency ω and wave number k are connected via phase velocity v. At $f \approx 0.1$ Hz the value of v was found to be close to the velocity of sound in the surrounding media: about 3000 m/s at LEP and about 2000 m/s at the SLC tunnel. For cultural noise this value decreases rapidly: the value of v determined from the SLAC data behaves as

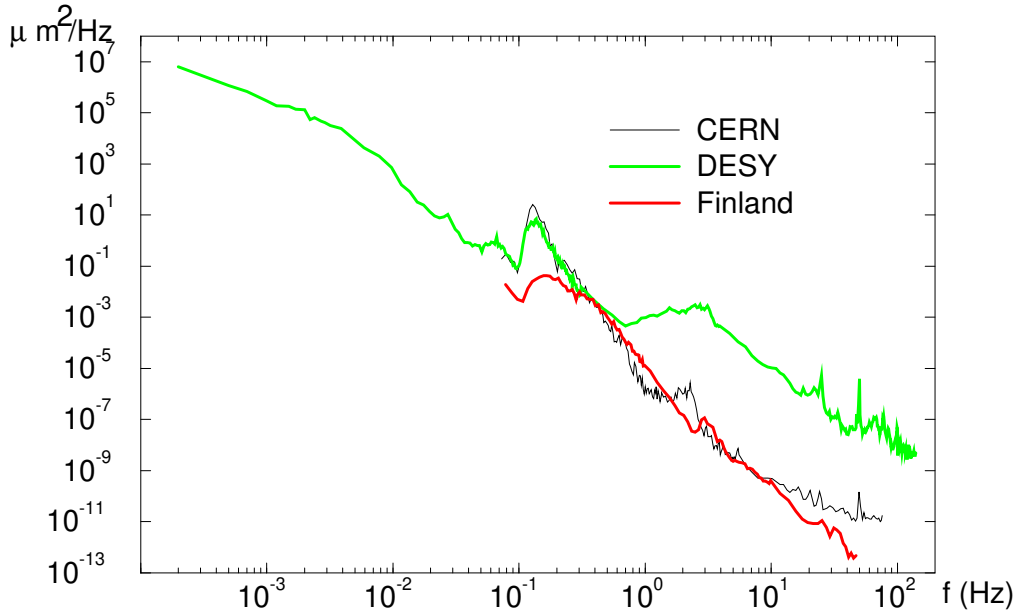

Figure 3.7.11: *Absolute power spectrum measured in quiet (CERN LEP tunnel, shutdown [6]; Finland, cave [7]) and noisy (DESY HERA tunnel, operational condition [8]) condition.*

$v \approx 450 + 1900\exp(-f/2\text{Hz})$ m/s (for $f > 0.1$ Hz) [10], HERA measurements gave $v \approx 400$ m/s [8]. The SLAC measurements have shown (at least at this place and these conditions) that the contribution of non-wave motion is negligible for $f > 0.1$ Hz.

The motion at $f < 0.1$ Hz is different. The elastic motion (produced by the moon, for example) is present here also, but of much bigger relevance is the inelastic diffusive motion, probably fed by the elastic motion and caused by its dissipation. The motion is believed to be described by the "ATL law" [5], which states that the relative rms displacement after a time T of the two points separated by a distance L is

$$\langle \Delta Y^2 \rangle = A\,T\,L$$

The parameter A was found to be $A \approx 10^{-6\pm1}$ $\mu\text{m}^2\text{s}^{-1}\text{m}^{-1}$ at different places. One can see that this displacement is proportional to the square root of the time and separation: this stresses the random, non wavelike, diffusive character of the slow relative motion.

The parameter A was observed to be smaller in tunnels built in solid rock. It also depends on the method of tunnel construction: in the tunnel bored in granite $A \approx 10^{-6}$ $\mu\text{m}^2\text{s}^{-1}\text{m}^{-1}$ was observed, while in a similar tunnel built by use of explosions, the parameter A is found to be 5 times larger probably because of the rock fragmentation, artificially increased during construction [9]. The high frequency correlation in the second case is also poor. The parameter A tends also to be smaller in deeper tunnels [13].

The ranges of T and L where the "ATL law" is valid are very wide. In [13] it was shown that "ATL law" is confirmed by measurements of ground motion in different

accelerator tunnels in the range from minutes to tens of years and from a few meters to tens of kilometers. The measured relative power spectra, presented in [9] and in [12], exhibit the "ATL" behavior for $f < 0.1$ Hz (for $L \approx 30$ m). These measurements indicate that the transition region from wave to diffusion motion is placed at rather short times (a few seconds). Measurements of the closed orbit motion in the HERA circular collider have shown that the power spectrum of this motion corresponds to the "ATL law" in a wide frequency range, from $f \approx 0.1$ Hz down to $f \approx 10^{-6}$ Hz and the parameter is $A \approx 10^{-5}$ $\mu\text{m}^2\text{s}^{-1}\text{m}^{-1}$ [12].

The very slow motion can be systematic (not described by power spectrum) as well. Such motion has been observed at LEP Point 1 and PEP [14] where some quadrupoles move unidirectionally during several years with rate about 0.1 – 1 mm/year. Points a few tens of meters apart can move in opposite directions. The amplitude of the motion can be larger than the one of diffusive motion. The motion is probably due to geological peculiarities of the place or due to relaxation if the tunnel was bored in solid rock.

The elements of the linac will be placed not on the floor, but on some girder, which could amplify some frequencies due to its own resonances. It is not only this amplification that is dangerous, more important is that the different girders can amplify or change the floor motion in different ways, and hence spoil correlation of the floor motion. It is therefore preferable to push the girder resonances to high frequencies where the correlation is poor anyway and floor amplitudes are smaller. This requires firm connections of the girder to the floor. The active systems [16], which can help to isolate the quadrupoles from high frequency human produced floor motion, should be made insensitive to slow motion (below 0.1...1 Hz), otherwise the correlation of long wavelength motion may be destroyed by imperfections of the active feedback when operating at low frequencies.

• **A model of the ground motion spectrum** $P(\omega, k)$ can be built [11] with the assumption that the low frequency part of motion is described by the "ATL law" [5], and the high frequency part is produced mainly by waves. The waves are assumed to be elastic, transverse, propagating at the surface of the ground with uniform distribution over azimuthal angle. The "ATL law" is included to the model in a modified form, in order to prevent overestimation of fast motion, which is an intrinsic feature of the pure "ATL law". The spectrum, which include both the waves and the modified "ATL law", is the following

$$P(\omega,k) = \frac{A}{\omega^2 k^2}(1-\cos(kB/A/\omega^2)) + \sum_i \frac{a_i}{1+[d_i(\omega-\omega_i)/\omega_i]^4}\,\frac{2}{\sqrt{(\omega/v)^2-k^2}}$$

We consider two set of parameters to cover two extreme cases of seismic conditions. Parameters of the first model are the following: $A = 10^{-5}$ $\mu\text{m}^2\text{s}^{-1}\text{m}^{-1}$, $B = 10^{-6}$ $\mu\text{m}^2\text{s}^{-3}$. The single peak described by $\omega_1 = 2\pi \cdot 0.14$ Hz for the frequency of the peak, $a_1 = 10\mu\text{m}^2/\text{Hz}$ for its amplitude, $d_1 = 5$ for its width, and $v_1 = 1000$ m/s for the velocity. This parameters represent quiet conditions.

The second model corresponds to seismic conditions with big contributions from cultural noises (as in the HERA tunnel in operating conditions). The parameters are

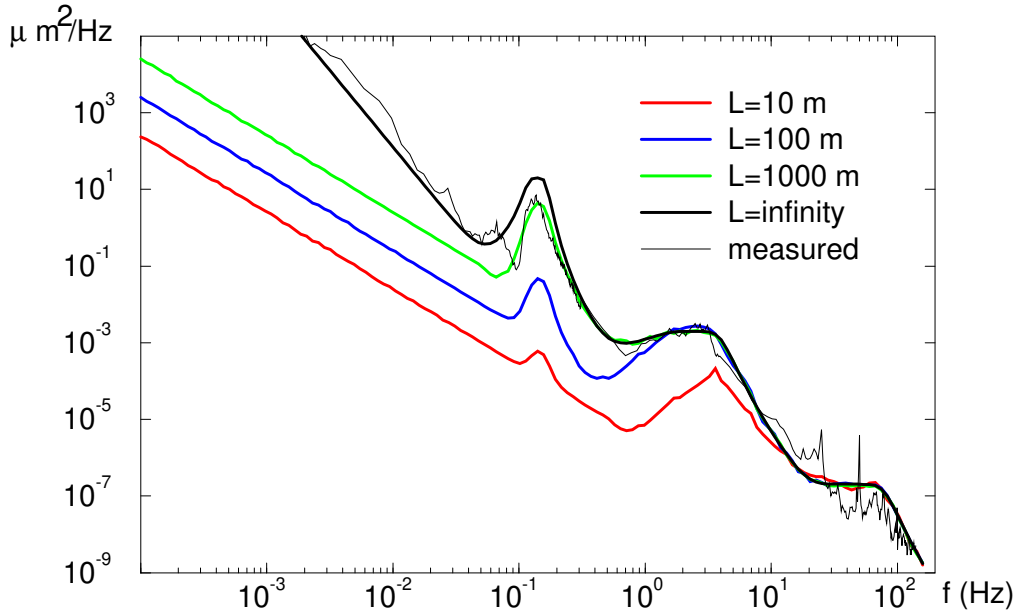

Figure 3.7.12: *Absolute power spectrum measured in a noisy conditions (HERA during operation [8]) compared to absolute and relative spectra for different spatial separation L calculated from the second model.*

the following: $A = 10^{-5}$ μm^{2}s^{-1}m^{-1}, $B = 10^{-3}$ μm^{2}s^{-3} and three peaks: $f_1 = 0.14$, $f_2 = 2.5$, $f_3 = 50$ Hz; $a_1 = 10$, $a_2 = 10^{-3}$, $a_3 = 10^{-7}\mu$m^2/Hz; $d_1 = 5$, $d_2 = 1.5$, $d_3 = 1.5$; $v_1 = 1000$, $v_2 = 400$, $v_3 = 400$ m/s. The corresponding spectrum of relative motion is shown on Fig.3.7.12.

• **Beam offset and spot size at the IP of TESLA** have been calculated analytically using the models of ground motion spectrum $P(\omega, k)$ and the corresponding spectral response functions, determined in linear approximation [11].

The most harmful effect of misalignments of focusing elements is the relative vertical offset of the opposite beams at the IP (Fig.3.7.13). The tolerance on the offset, corresponding to 2% luminosity loss, is around 5 nm for TESLA. It corresponds to critical times around 1 s for the quiet model and 1 ms for the (likely somewhat too pessimistic) noisy model. This means that even in the extremely noisy conditions the fast orbit feedback, described in section 3.8.3, will be able to keep the beams colliding.

Transverse displacements of focusing elements generate spot size growth at the IP induced by dispersion, longitudinal shift of the beam waists and xy-coupling generated by offsets of the beams in quadrupoles and sextupoles. Corresponding spectral response functions have been calculated and the beam size growth due to all these effects has been determined (Fig.3.7.14). The main contribution to the vertical beam size growth comes from yx' coupling and from vertical dispersion. One can see that the critical time scale for 2% luminosity loss is about 200 s that imposes quite relaxed requirements to the beam size stabilization feedback described in the next section.

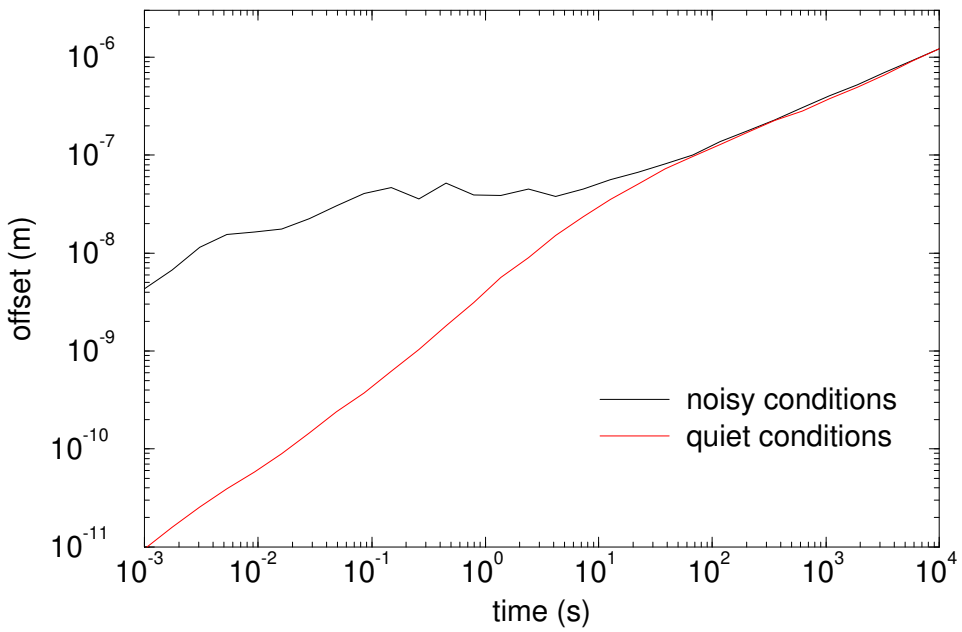

Figure 3.7.13: *Relative vertical rms offset of the beams at IP of the TESLA Beam Delivery system for the noisy and quiet models of the power spectrum of ground motion.*

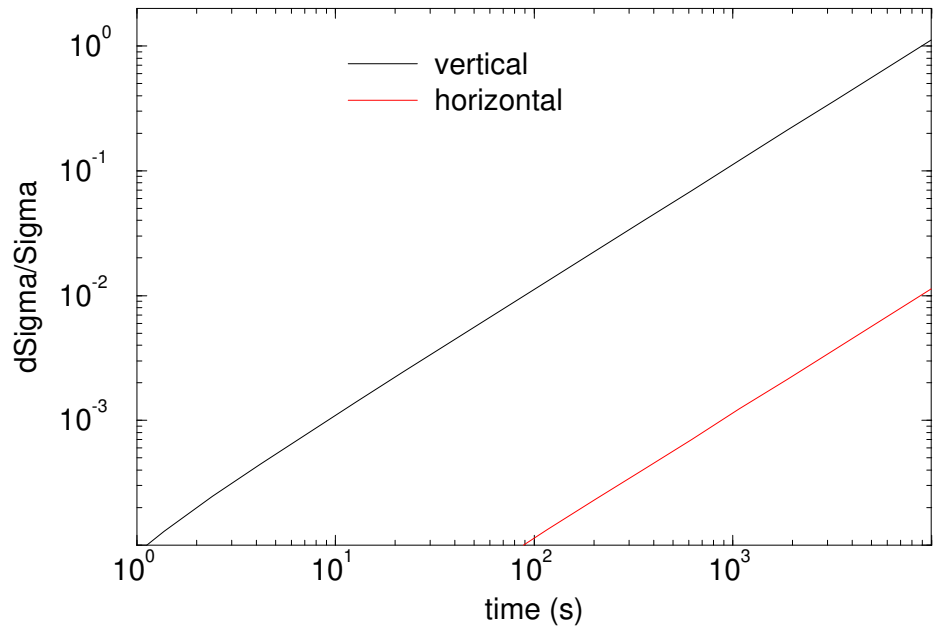

Figure 3.7.14: *Vertical and horizontal rms beam size growth $\delta\sigma^*/\sigma^*$ versus time for the "ATL" ground motion with $A = 10^{-5}\ \mu m^2 s^{-1} m^{-1}$. Rms energy spread of the beam is $\delta p/p = 10^{-3}$.*

3.7.5 Phase Space Measurement and Tuning

3.7.5.1 Introduction

With the experience gained from two existing final focus systems (SLC and the final focus test beam, FFTB), the various tuning techniques which are required to produce the small beam sizes at the IP are already mature and well tested. For the next generation of linear colliders, the tuning used at the FFTB [18] is particularly relevant. In the following sections, we will discuss the application of these and other tuning techniques to the TESLA beam delivery system.

3.7.5.2 Energy Measurement and Correction

The beam delivery system offers several near optimum positions for the precise measurement of the relative energy (momentum) error of the bunches. Both the collimation sections and the chromatic correction sections have symmetric high dispersion points positioned by a *-I* transformation apart in betatron phase space, allowing any betatron component of the horizontal beam offset at these points to be effectively canceled out by taking the sum of the two measurements. The resolution of such a system is given by (a) the value of the dispersion function (b) the resolution (noise) of the BPM and (c) the accuracy of the cancelation of the betatron component. Table 3.7.2 gives the relevant parameters for the four sets of symmetric dispersion points available in the TESLA beam delivery system. The resolution is calculated assuming the given BPM precision (5 μm) and a (conservative) random beam jitter of $\sigma/4$.

section	D_x (mm)	β_x (m)	σ_x (μm)	σ_{BPM} (μm)	resolution
collimation	47	1157	182	3	10^{-4}
CCS X	35	881	159	5	10^{-4}
CCS Y	35	26.5	28	5	10^{-4}

Table 3.7.2: *Key parameters for -I paired BPMs used as spectrometers in the beam delivery section. The collimation section refers to both the sine- and cosine-like sections which have identical parameters.*

Either of the two BPM pairs in the collimation sections can be used in a fast energy feedback system to correct the bunch to bunch energy error before entering the final focus section. Such an arrangement is shown schematically in figure 3.7.15. By placing the correction RF cavities downstream of the measurement BPMs, a signal delay time of the order of 0.1 μsec can be achieved (assuming a cable signal velocity of approximately $0.8c$). By performing all the necessary signal processing in hardware it should be possible to make an energy correction within the TESLA bunch spacing (0.7 μsec). The system can also be used as a low bandwidth feedback to compensate slow drifts. In this case the correction can be performed at the exit of the linac using

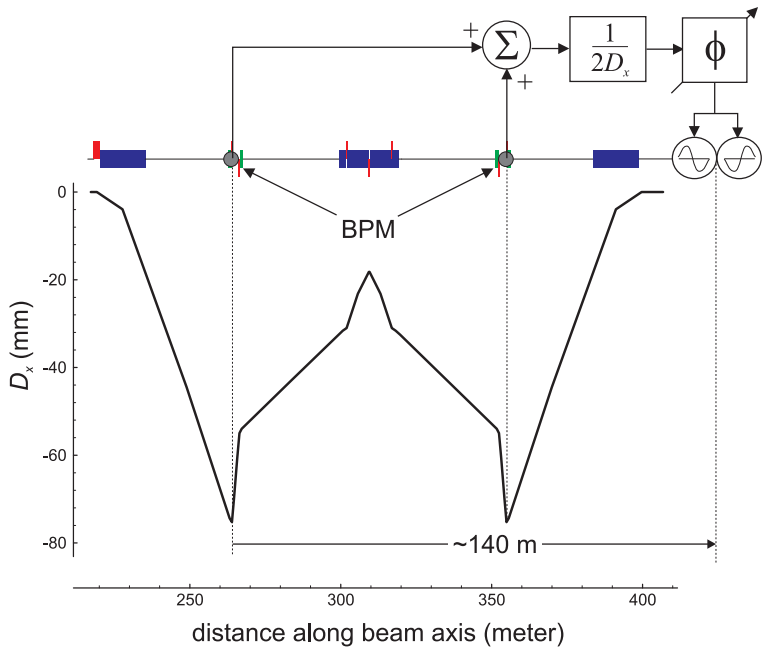

Figure 3.7.15: *Fast energy correction scheme (feedback). Two back-phased cavities are used to cancel the energy spread induced along the bunch length from the (nominally) zero phase crossing of the RF*

existing cavities, and no additional (fast) cavities are required in the beam delivery section.

3.7.5.3 Beam Based Alignment

The most critical aspect of the initial final focus tuning is the alignment of the magnets. The strong quadrupoles and sextupoles within the system have tight tolerances that must be met in order to reduce optical aberrations below the acceptable values. Since the alignment tolerances are tighter than can probably be achieved using conventional survey techniques, the position of the magnets must be corrected using the beam based alignment techniques already successfully demonstrated at the FFTB [19].

By using individual power supplies, the excitation of each magnet is changed and the resulting difference in downstream orbit is recorded, from which the relative offset of the magnet with respect to the beam can be estimated. Each magnet (excluding dipoles) is placed on a remotely translatable stage (magnet mover) which enables the precise (sub-micron) positioning of the magnet [20]. With high precision BPMs , alignment precisions on the order of 3 μm should be feasible. The strong Sextupoles can be aligned using the waist shift techniques first demonstrated successfully at the SLC [21].

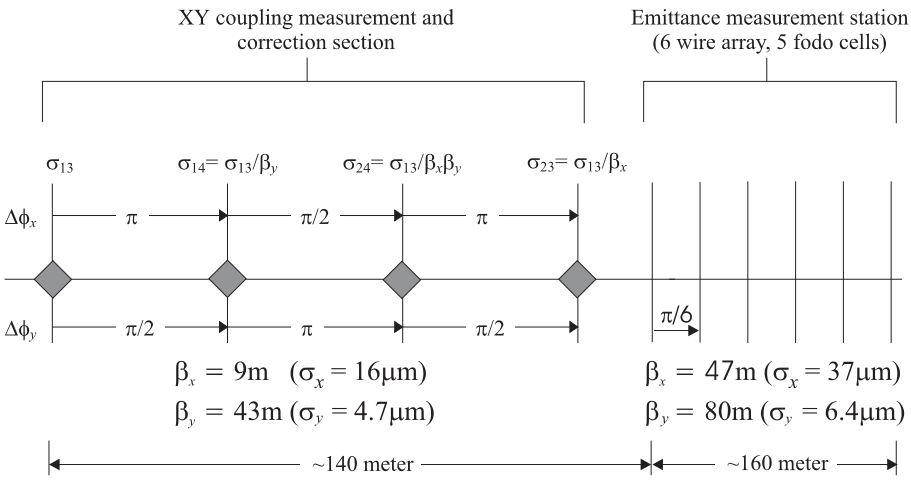

Figure 3.7.16: *Schematic of coupling measurement and correction section together with the downstream six wire array emittance measurement section. The fodo parameters for the emittance measurement station are chosen to give a 1% measurement resolution (assuming a 1 μm rms wire).*

3.7.5.4 Coupling Correction

With emittance ratios of 50:1 it is important to reduce any cross plane (X-Y) correlations in the 4-dimensional beam phase space. The linear correlations ($\langle xy \rangle$, $\langle xy' \rangle$, $\langle x'y \rangle$ and $\langle x'y' \rangle$ can be completely removed with four skew-quadrupoles placed at non-degenerate phases. There are two possible correction schemes that can be applied:

1. measure the correlations and adjust the four skew-quadrupoles accordingly.

2. generate a set of four orthogonal coupling knobs, and minimise the vertical emittance as a function of each in turn [23],

In TESLA, both possibilities are supported in a single tuning section. The lattice shown in figure 3.7.16 is chosen to make each single skew-quadrupole correct an independent coupling term (i.e an orthogonal knob) [23]. Immediately downstream of the skew-quadrupoles is a 6-wire emittance measurement section as described in [22], which is capable of a relative emittance measurement error of approximately 1%. The vertical emittance is minimised as a function of each skew-quadrupole strength in turn. It should be noted that the skew-quadrupoles are only orthogonal over a limited range around zero: should a large amount of correction be required, then the procedure must be iterated.

The orthogonal split-phase lattice utilised for the coupling correction also affords an elegant de-coupled measurement of the four individual X-Y correlations. Four wire scanners are placed at the same locations as the skew-quadrupole as discussed in [22]. Each wire scanner has an additional angle wire (the u-wire), which together with the horizontal and vertical wire measurements can be used to determine the $\langle xy \rangle$ correlation

of the beam at that wire scanner. At each wire scanner location, the measured $\langle xy \rangle$ correlation relates directly to an individual correlation term of the beam as measured at the first wire scanner (as shown in figure 3.7.16). Together with the downstream emittance measurement station, the coupling measurement station allows the complete determination of the 4-dimensional phase volume, the results of which can be used to determine the settings of the matching quadrupoles (skew and normal) with the aid of some suitable optics program, preferably on-line.

3.7.5.5 Beta Matching

By design, a final focus system for a linear collider contains large chromatic elements which are so positioned as to cancel the resulting aberrations. Given the delicate balance of this cancelation and the subsequent tolerances of the components, it is highly desirable to limit the amount of tuning which takes place within the final focus to a minimum: the IP tuning should be considered as a final fine tuning of the IP phase space (see section 3.7.5.6). To facilitate this, care must be taken to make sure that the incoming phase space is matched correctly to the final focus. The wire array system described in section 3.7.5.4 allows the determination of the full 4-dimensional phase volume, from which the setting of the a) skew-quadrupoles in the coupling correction section and b) the normal quadrupoles in the downstream β-matching section can be determined. As an additional cross check, a single wire scanner can be placed at the IP image point at the entrance of the horizontal chromatic correction section. If the final focus lattice is correctly adjusted, then a waist at this wire scanner corresponds directly to a waist at the IP. Waist scans can be made at the wire by driving six upstream quadrupoles in the correct (non-linear) fashion[26]. Assuming the coupling has already been corrected, the β-function at the image point can be obtained from the waist scan information, and a subsequent adjustment made to obtain the correct beam size. For the design vertical emittance the vertical beam size at the image point is 952 nm ($= 50 \times \sigma_y^*$), the measurement of which is well beyond the carbon fiber limit and will require laser technology or possibly a gradient undulator beam size monitor[24].

3.7.5.6 IP tuning

The final focus optics must first be checked and if necessary adjusted to given the correct box-structure lattice. Specifically the -I sections between sextupoles in the chromatic correction sections must be measured using the corrector-BPM null method outlined in [18]. Additional wire scanners at the intermediate IP image points can be also used to check the consistency of the optics (since they should all measure the same beam size). Unfortunately the beam sizes at these downstream image points have a large contribution from the chromaticity generated by the CCS sextupoles, and so it will be necessary to turn the sextupoles off during the measurement.

Final (linear) tuning of the IP phase space requires in principle six orthogonal knobs:

1. X and Y waist IP shift,

2. X and Y IP dispersion,

3. $\langle xy \rangle$ and $\langle x'y \rangle$ coupling.

For the last case (coupling), only the $\langle x'y \rangle$ is important, since there is no generating term for the $\langle xy \rangle$ correlation due to the single phase nature of the lattice (this assumes that the incoming coupling has been corrected using the techniques described in section 3.7.5.4). The remaining coupling term can be tuned out using a single skew-quadrupole placed close to the final doublet, or using the sextupole mover technique discussed below.

All five required tuning knobs can be easily generated using transverse displacement of the sextupole pairs in the CCS. This technique is particularly appealing since errors in alignment of the sextupoles are expected to be a significant source of the aberrations we wish to use them to correct. For a given sextupole pair, the transverse offset (horizontal and vertical) can be driven symmetrically or anti-symmetrically. The two sets of sextupoles movers can be ganged together to produce orthogonal X and Y knobs (for the waist and dispersion correction). Table 3.7.3 shows the various knob combinations while table 3.7.4 gives the numerical parameters. Exactly the same effect can be achieved by placing small normal and skew quadrupoles at the sextupoles and ganging the power supplies in pairs.

	symmetric	a-symmetric
horizontal	waist shifts	horizontal dispersion
vertical	$\langle x'y \rangle$ and $\langle xy' \rangle$	vertical dispersion

Table 3.7.3: *The four combinations of sextupole movers and their effect at the IP.*

		X	Y
X CCS	waist	830	2.4
	dispersion	6.2	0.33
	coupling	44.5	
Y CCS	waist	129	355
	dispersion	0.34	3.3
	coupling	215.	

Table 3.7.4: *Coefficients for the various mover combinations given in table 3.7.3. The coefficients are per unit sextupole offset.*

The typical amount by which the sextupoles must be displaced depends on the size of the scan range and subsequent correction necessary. As a good guideline, we assume

that a scan range is such that it increases the effective IP β-function by a factor of three (i.e. it increase the beam size by a factor of $\sqrt{3}$). Combining the above coefficients into orthogonal knobs, table 3.7.5 gives the amount of transverse motion of each sextupole to complete a 3β scan (for the coupling, only the vertical beam size is scanned using the vertical CCS sextupoles). Mechanical movers of a similar design as those developed for the FFTB [20] should be adequate given the requirements in table 3.7.5.

	CCS X (μm)	CCS Y (μm)	motion
x-waist	42.	-0.29	horizontal
Y-waist	-0.44	2.82	horizontal
x-dispersion	191	-19.1	horizontal
y-dispersion	-0.42	7.6	vertical
coupling		3.5	vertical

Table 3.7.5: *Expected motions of the sextupole pairs in the X and Y CCS to give orthogonal 3β scans at the IP.*

All the tuning described above requires some measurement of the beam size at the IP. While colliding beams are available, beam-beam scans can be used as a tuning signal, as can any fast luminosity signal. It is considered essential that a single beam diagnostic be available at or near the IP for initial tuning and fault diagnostics. A laser interferometer beam size monitor[25] will be placed some 80 cm along the beam axis from the actual IP. The focal point of the beam must be moved to the location of the the laser monitor requiring an adjustment of the β-match (a waist shift). Such a waist shift is easily produced by the sextupole pairs as previously mentioned (a symmetric horizontal displacement of 360 μm for X and 845 μm for Y).

3.7.6 Orbit and Spotsize Stabilisation

The alignment tolerances in the beam delivery system are some of the tightest in the machine. While it is expected that initial beam-based alignment can achieve these tolerances, the question still remains how stable the system is over time, given that ground motion will slowly displace all the components from their ideal positions. The effects of ground motion on the luminosity can be separated into three distinct time scales:

1. displacement of the beams relative to each other at the IP
2. dilution of the IP beam sizes by linear optics aberrations
3. dilution of the IP beam sizes by non-linear optics aberrations.

The relative displacement of the beam at the IP has the shortest time constant: if the effects of ground motion are left uncorrected, the luminosity drops rapidly as

the beams move out of collision. Assuming that this offset is corrected using the proposed fast feedback system (section 3.8.3), the next effect is that of linear optics aberrations increasing the beam size at the IP. As the ground motion displaces the magnets, the RMS of the beam trajectory through the system will increase rapidly, generating spurious dispersion, IP waist shifts and X-Y coupling (the latter two effects coming from the strong sextupoles in the chromatic correction sections). These effects can be dramatically reduced by routinely re-steering the beam delivery systems. In addition, the linear IP tuning knobs can be scanned during routine luminosity operation to remove any residual linear aberration not corrected by the steering (see section 3.7.5.6). Once (1) and (2) are corrected, the only remaining effects are non-linear aberrations (most notably non-linear dispersion). When these effects become large enough to reduce the luminosity below an acceptable limit, then the beam delivery system will require invasive tuning, and most probably a re-alignment of the magnets (using beam-based alignment).

To study the effects of ground motion and how effective the various tuning and orbit correction strategies are, a purpose built simulation tool known as MERLIN has been developed at DESY. The MERLIN model of the TESLA beam delivery system has the following key points:

1. both electron and positron systems are simulated, and the luminosity is calculated from the results of particle tracking through both (independent) models

2. ground motion (ATL) is applied to both electron and positron models in a consistent way to obtain the correct correlations between the two

3. components can be placed on girders (supports), and will then move together under the influence of ground motion

4. each magnet has an associated BPM, both of which are placed on magnet movers (which in turn are placed on a support).

Figure 3.7.17 show recent result of the MERLIN TESLA BDS model. The three graphs shown are the averaged results of running twenty random seeds for the ground motion, with $A = 10^{-5}\mu m^2/m/s$. The logarithmic time scale represents thirty days of running. The first graph (a) shows the effect of ground motion alone with no tuning, from which it is clear that the luminosity drops below an acceptable level within seconds. The second graph (b) shows how the effect of the IP steering feedback stabilises the luminosity by keeping the beams in collision. The critical time for luminosity loss is now of the order of one hour. The final graph (c) shows the effects of so-called one-to-one orbit correction: the beam is steered to zero the beam offset in all the BPMs (and consequently the centres of the their associated magnets). Particular care is taken to steer to the centre of all sextupole magnets and the final doublet (in the latter, a single BPM placed between the two doublet magnets is used). The result indicates that a 5% drop in the luminosity after after thirty to forty days can be expected (due to residual non-linear effects, most notably non-linear vertical dispersion). Result (b) suggests

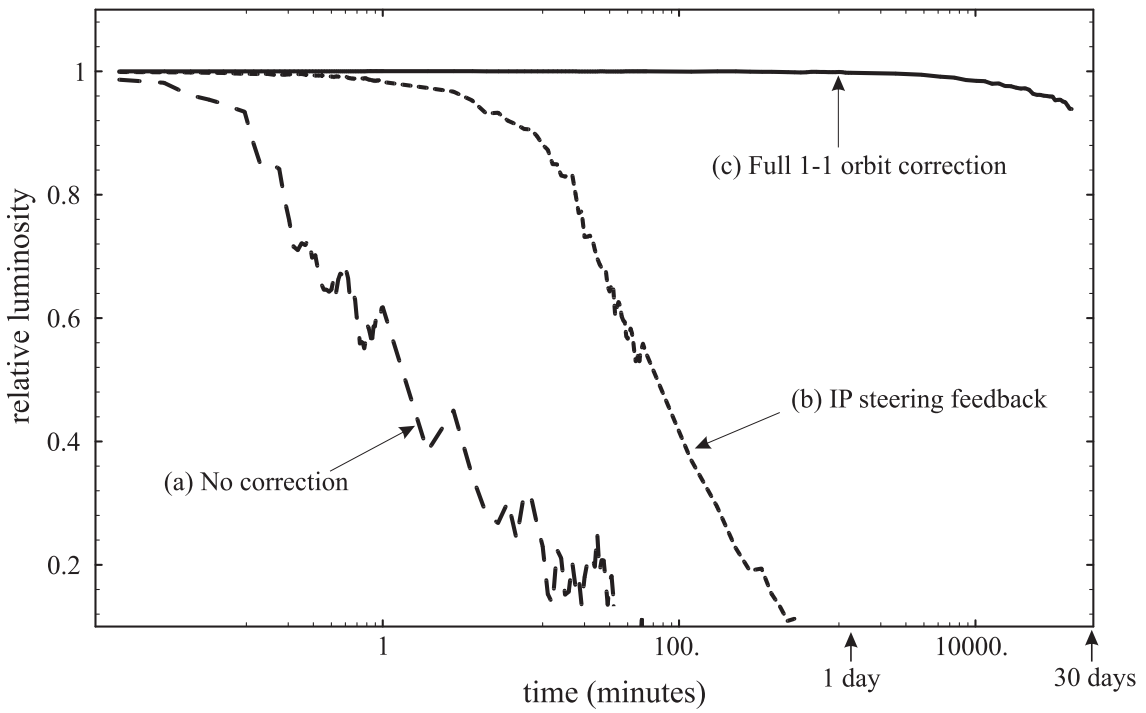

Figure 3.7.17: *Simulations of luminosity (relative to the design value) as a function of time. Three separate simulation runs are shown depicting (a) no correction, (b) IP beam offset correction (IP steering feedback) and finally (c) full 1-to-1 orbit correction of both electron and positron beams (see text for additional details).*

that such an orbit correction is only necessary approximately once every thirty minutes or so, giving the correction system plenty of time to average many pulses, eliminating the need for extremely high precision (i.e. nanometer-type) BPMs.

Given the current results, it is expected that the TESLA beam delivery system will require an invasive re-tuning (i.e. beam-based alignment) at intervals of approximately thirty to forty days. While this is acceptable, it is expected that use of better steering algorithms, tuning schemes and non-linear knobs can extend the time between re-alignment.

3.7.7 Beam-Beam Effects

The two colliding bunches focus each other at the interaction point, reducing the effective beam cross section compared to the nominal one. The actual luminosity is thus larger than the geometrical one by the pinch enhancement factor H_D. Due to the bending of their trajectories the particles emit a radiation called beamstrahlung. The resulting energy loss smears the luminosity spectrum and has thus to be limited, which in turn limits the achievable luminosity. The resulting spectrum is especially important for studies of the top quark at threshold and is discussed in the appropraite section in more detail.

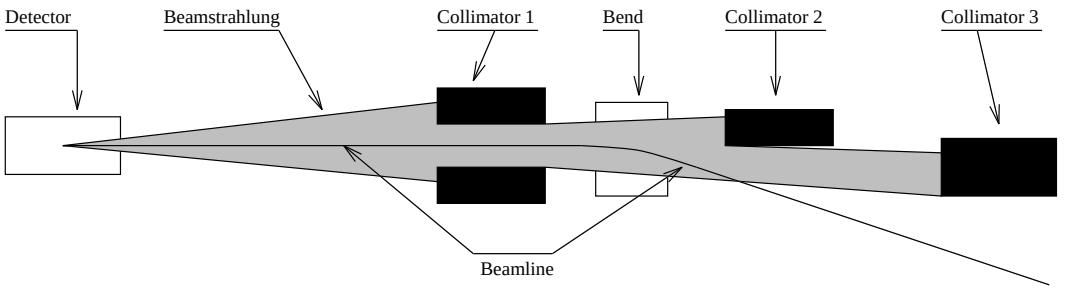

Figure 3.7.18: *Sketch of the beamstrahlung collimation*

The strong bending of the trajectories requires a numerical simulation to estimate the actual luminosity and the beamstrahlung. The numbers in the following are obtained using the computer code GUINEA-PIG [27]. For the standard beam parameters of TESLA the simulations yields a luminosity of $6 \cdot 10^{33}\,\mathrm{cm}^{-2}\mathrm{s}^{-1}$ ($H_D = 1.6$) and an average relative energy loss of the beam particles of $\delta = 2.5\%$. The total power of the beamstrahlung of one beam is about 200 kW.

The beamstrahlung is emitted into a small cone in the forward direction of the beams. Its angular spread is dominated by the angular spread of particles in the bunches during the interaction and the core is well below 500 μrad. The photons therefore pass the final quadrupoles safely. Since the beams collide head-on in TESLA, the magnets of the final focus system on the other side have to be protected from the beamstrahlung. Therefore three collimators are used, the first of which has to intercept most of the power—see Figure 3.7.18. The large distance between the final doublet and the closest magnets in the final focus system allows to collimate at a distance of 90 m from the interaction point. The collimator has a small inner radius of 4 mm to also collimate the synchrotron radiation emitted by the incoming beams, which form a significant background source in SLC.

The collimators consist of a titanium beam pipe with a thickness of 0.5 mm surrounded by water longitudinally flowing at a speed of 3 m/s. Simulations show that the stress induced when the photons heat up the titanium, is an order of magnitude below the endurance limit [27]. The direct temperature increase of the water is well below 10 K.

In the collimator neutrons are produced by the photons in the electro-magnetic showers. The flux at the position of the detector would be about $8 \cdot 10^{11}\,\mathrm{cm}^{-2}$ per year. The main detector be shielded with a concrete wall, 5.5 m reduce the flux to less than $4 \cdot 10^{6}\,\mathrm{cm}^{-2}\mathrm{y}^{-1}$ or 1 μSv/h. The vertex detector is less easy to shield since the wall must have a hole for the beams. With the mask inside the detector described in chapter 2 the flux of neutrons in the detector can be suppressed by more than three orders of magnitude to less than $10^{9}\,\mathrm{cm}^{-2}\mathrm{y}^{-1}$.

The beamstrahlung also increases the background produced in the interaction point. An important contribution to the background are the three processes creating $\mathrm{e^+e^-}$-pairs: $\mathrm{ee} \to \mathrm{ee(e^+e^-)}$, $\gamma\mathrm{e} \to \mathrm{e(e^+e^-)}$ and $\gamma\gamma \to \mathrm{e^+e^-}$, where the real photons are due to beamstrahlung. The pair particles are produced mainly at small angles with respect to the beam axis but since their energy is small their trajectories are strongly bent by

E_{cm}	[GeV]	500	500 low ϵ_y	800	800 low ϵ_y	1600
L	$[10^{33}\,\mathrm{cm}^{-2}\mathrm{s}^{-1}]$	6.0	8.4	5.7	11.1	22.4
δ	[%]	2.5	0.95	5.2	2.2	6.1
N_P	$[10^3]$	96	51	180	104	230
E_P	$[10^3\,\mathrm{GeV}]$	164	71	650	310	2200
$N_\perp$		31	15.8	46.5	28	50
$N'_\perp$		31	15	49	27	41
N_{Hadr}		0.13	0.06	0.46	0.19	0.87
N_{MJ}	$[10^{-2}]$	0.3	0.15	1.6	0.7	6.9

Table 3.7.6: *Luminosity L average energy loss δ and background for different TESLA parameter sets. N_P pair particles with a total energy of E_P are produced per bunch crossing, $N_\perp$ of which have transverse momentum in excess of* 20 MeV *and an angle with respect to the beam axis of more than* 150 mrad. *$N'_\perp$ is the number of particles per bunch crossing that will not enter the masks—without taking the deflection by the beams into account (which gives a value about* 20% *higher in the case of TESLA500). The number of hadronic events is N_{Hadr} including N_{MJ} minijet pairs with a transverse momentum of more than* 3.2 GeV.

the fields of the beams. If a particle moves in opposite direction of the bunch with the same sign of charge, it is deflected by the fields to a maximal angle depending on its energy.

Simulation with GUINEA-PIG predicts the production of about 10^5 particles with a total energy of $1.6 \cdot 10^5$ GeV per bunch crossing in TESLA. Most of these particles hit the final quadrupoles where they produce secondary photons and neutrons. The detector is shielded from the photons by a tungsten mask. In Table 3.7.6 the number of particles with a transverse momentum of more than 20 MeV and an angle of more than 150 mrad is given. This number is about 31 per bunch crossing. The numbers for other parameter sets can also be found in Table 3.7.6.

Single bremsstrahlung ee $\rightarrow$ eeγ is another process leading to low energy particles. It can be used to measure luminosity, but since the particles can loose a significant amount of energy they are strongly over-focussed by the oncoming beam and can therefore be lost in the final quadrupoles. The simulation yields a total energy deposition in the final quadrupoles by these particles of about $2 \cdot 10^5$ GeV per bunch crossing.

The rate of hadronic two photon events is 0.13 per bunch crossing with a photon-photon centre of mass energy in excess of 5 GeV. The visible energy of each of these events is about 10 GeV.

3.7.8 Beam Collimation

In order to avoid that the detector can be blinded by background produced from large amplitude halo particles in the interaction region, the trajectory amplitudes have to be restricted such that (a): the entire beam remains within the aperture of the final

quadrupoles in front of the IP and (b): the synchrotron light produced by particles with large offsets in the final doublet (FD for short) can pass freely through the aperture of the doublet downstream from the IP. The second condition is more stringent than the first and we lay out the collimation system according to this boundary condition. With its large aperture radius of 24 mm, the superconducting doublet can accomodate outgoing synchrotron light produced by particles with amplitudes as large as 12 horizontal and 48 vertical standard deviations for the standard parameters at 500 GeV. It is unlikely that in the TESLA linac tails reaching out to such large amplitudes can be populated. Scattering from gas molecules is almost not present in the superconducting structures and wakefield effects are small. Dark current is expected to be low with field emission being suppressed by careful processing of the cavities and furthermore field emitted particles which are accelerated are swept away by the next quadrupole(s) downstream. Beam halo produced in the damping ring can be scraped off before injection into the main linac. Therefore, including an efficient collimation system in the beam delivery design provides a large amount of safety to protect the interaction region from unwanted background.

3.7.8.1 Layout of the System

In principle, only large amplitude trajectories at the FD-phase are harmful, since the acceptance for IP-phase trajectories is orders of magnitude (in units of σ's) larger. FD-phase collimation can easily be provided at the high-β positions in the final focus system (FFS). However, being relatively close to the IP, muons originating from the FFS-collimators can reach the detector with high probability and the tolerable amount of beam halo scraped off in the FFS would be small. We therefore include a first collimation stage farther away from the IP, inserted between the end of the linac and the tuning and diagnostic section. Only a small fraction of halo particles escaping from the primary system will then hit the secondary collimators in the FFS.

In this scheme, one must take into account the possibility of trajectories changing amplitude and phase due to aberrations in the beam optical system between the 1st stage collimators and the FD. This leads to the requirement that collimation at both the FD and the IP phase is necessary and that the collimator aperture must be smaller by about a factor of 1.5 compared to the FD acceptance defined above. The resulting layout of the 1st stage system is sketched in fig. 3.7.19. Two pairs of spoilers, placed at high β and high dispersion points in the lattice, provide simultaneous collimation in x, y and $\Delta p/p$. The first pair collimates at the IP-phase, the second one at the FD-phase. We follow here a concept of mechanical collimation originally developed at SLAC [28]. The spoilers are thin (about 2 R.L. Titanium, see below) and act to increase the angular and momentum spread of the part of the beam outside the acceptance while 20 R.L. Cu-absorbers downstream catch the halo emerging from the spoilers. An overview of the spoiler and absorber parameters is given in table 3.7.7. The secondary collimators in the FFS are set to apertures corresponding to $12\sigma_x$ and $48\sigma_y$ and are safely in the shadow of the primary system.

The overall efficiency of the system is tested by particle tracking calculations using

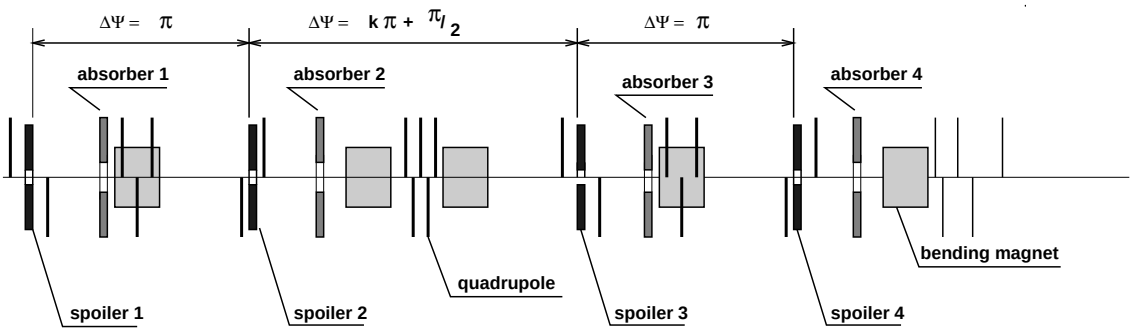

Figure 3.7.19: *Sketch of the 1st stage (main) collimation system.*

element	SPOILERS				ABSORBERS			
number	1	2	3	4	1	2	3	4
half gap g_x [mm]	1.3	1.3	1.3	1.3	2.30	2.73	2.30	2.73
half gap g_y [mm]	1.9	1.9	1.9	1.9	3.30	2.68	3.30	2.68
# of σ_x	8	8	8	8	30	30	30	30
# of σ_y	32	32	32	32	100	100	100	100
acceptance $\Delta p/p$ [%]	3.2	3.2	3.2	3.2				

Table 3.7.7: *Apertures of the main collimation system spoilers and absorbers.*

the STRUCT code [29]. The beam halo is simulated by a $|x|^{-1} \cdot |y|^{-1}$ particle distribution outside the collimator aperture. The efficiency of the primary stage is shown in fig. 3.7.20 as a function of spoiler length. For 2 R.L. Titanium, a fraction of 5×10^{-5} of the simulated beam halo escapes from the system. In the simulation all of these particles are stopped in the 2nd stage collimators. From the tracking results we estimate that less than 10^{-7} of beam halo particles have a chance to produce a hit in the interaction region quadrupoles with the conservative assumption that the efficiency of the 2nd stage collimators is 10^{-3}. For one hit per bunch crossing, a beam loss of up to about 0.03% in the collimators would be tolerable, far in excess of a conceivable halo population of the beam. The average synchrotron radiation power deposited in the interaction region for such an unrealistically high beam loss is estimated as 0.006 mW, roughly 6 orders of magnitude smaller than without any collimation.

3.7.8.2 Spoiler Protection

Though the beam is enlarged at the spoiler position by optical magnification it still exhibits an enormous power density of $P_{tot}/2\pi\sigma_x\sigma_y \approx 140$ MW/mm^2. Of course there is no material which could withstand such a power density for a longer time. On the other hand the spoilers are close to the beam and one has to take into account the possibility that a mis-steered beam hits the spoiler head on. In that case the enhanced loss rates trigger a kicker upstream which extracts the bunchtrain from the main beamline. The extracted beam is then guided to the main beam dump (see section 3.7.9). In order to allow a few μs reaction time for the safety system, the spoilers still have to accept the

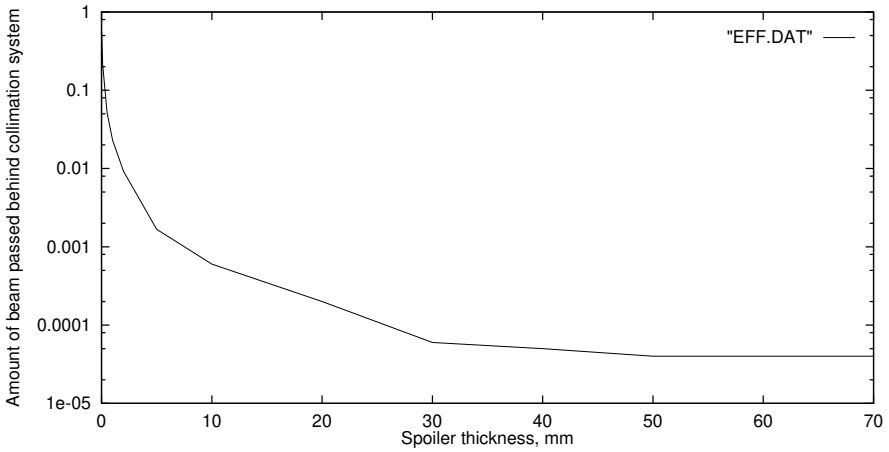

Figure 3.7.20: *Fraction of beam halo escaping from the primary collimation system as a function of spoiler thickness. For Titanium 2 R.L. correspond to 70 mm.*

	$(dE/dx)_{min}$ [MeV/cm]	ρ [g/cm^3]	$c(T = 298\text{K})$ [J/gK]	λ [W/cmK]	X_0 [cm]
Ti	6.85	4.54	2.0	0.15	3.56
C	4.0	2.20	0.71	2...3	19.3

Table 3.7.8: *Some properties of pyrolytic graphite and titanium.*

loss of several bunches.

We consider here two possibilities - a titanium spoiler and a graphite spoiler. Properties of both materials are given in table 3.7.8.

Due to the large radiation length the graphite spoiler is much longer compared to titanium. This leads to a larger transverse spread of the induced shower in graphite and results in a lower maximum energy deposition. In order to determine the instantaneous temperature jump due to the deposited energy one has to take into account the temperature dependence of the heat capacity:

$$\frac{dE}{dm} = \int_{T=T_0}^{T_0+\Delta T_{inst}} c(T)dT. \tag{3.7.1}$$

The instantaneous temperature jump ΔT_{inst} can be calculated by solving (3.7.1) numerically. Parameterizations for $c(T)$ can be found in [30], temperature curves for both materials are shown in fig. 3.7.21.

The heating induces thermal stresses in the material which, if too high, will lead to cracks and damage the spoiler. The temperature limit can be estimated from the induced stresses:

$$\sigma_{UTS} > \frac{1}{2}\alpha E \Delta T_{inst}. \tag{3.7.2}$$

Here one should take into account that the material dependent parameters σ_{UTS} ultimate tensile strength, α linear expansion coefficient and E elastic modulus are also

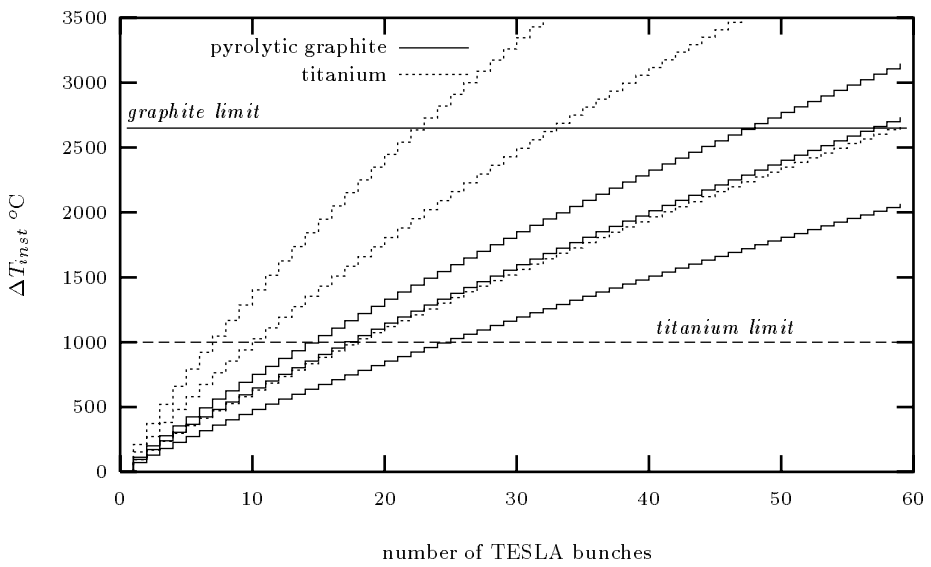

Figure 3.7.21: *Instantaneous temperature rise in graphite and titanium as a function of the number of TESLA bunches hitting the spoiler. The three curves for each material correspond to a thickness of 1.0, 1.5, 2.0 radiation lengths.*

functions of temperature. From (3.7.2) we estimate limits of $\approx$ 1000 °C for Ti and 2650 °C for pyrolytic graphite. From the temperature curves in Figure 3.7.21 it can be concluded that both materials are suited for a beam spoiler and can withstand a sufficient number of bunches. However, a two radiation length thick pyrolytic graphite spoiler can accept nearly 50 bunches on the same spot whereas the equivalent titanium spoiler stands only 6 bunches. The passage time of 6 bunches is 4.2 μs which is sufficient to trigger the safety system. Still a graphite spoiler would promise a higher inherent safety in case of accidental beam losses. Another advantageous property of graphite is its large thermal conductivity λ which becomes important if relatively large steady beam losses on the spoilers have to be handled. Such a situation is imaginable for instance during set-up and tuning of the machine.

3.7.8.3 Emittance Dilution by Wakefields

Ultrarelativistic particles moving in a perfectly conducting pipe experience no transverse kick since the forces caused by the electric and magnetic field cancel exactly. However, at discontinuities as the entrance or the exit of a beam spoiler this cancelation is distorted and particles in an off-axis bunch will experience an effective kick due to the induced fields. The so called geometric wake field kick varies along the longitudinal direction of the bunch and can be estimated for rectangular spoilers by [31]:

$$\Delta y'(z) = \theta_1 \exp\left(-\frac{z^2}{2\sigma_z^2}\right)^1; \quad \theta_1 = \frac{\pi^2 r_e N_B}{2\sqrt{2\pi}\gamma\sigma_z}\frac{\langle \Delta y\rangle}{g}, \tag{3.7.3}$$

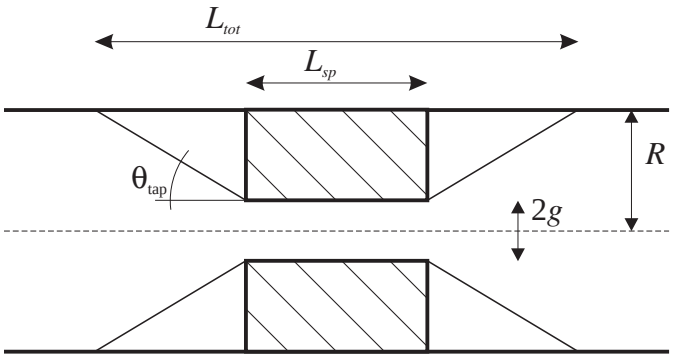

Figure 3.7.22: *Sketch of the tapered spoiler.*

where $r_e = 2.8 \cdot 10^{-15}$ m the classical electron radius, $\sigma_z = 0.7$ mm the rms bunch length, $N_B = 3.6 \cdot 10^{10}$ the bunch population, $\langle \Delta y \rangle$ the transverse bunch offset and g the half gap between the spoilers.

Since the strength of the kick varies along the bunch it dilutes the beam emittance. We assume that the mean kick can be corrected with steering elements and demand a luminosity reduction of less than 2 % for one σ_y offset at the spoiler:

$$\frac{\Delta L}{L} = \frac{1}{2}\frac{\Delta \varepsilon}{\varepsilon} = \frac{1}{2}\frac{\Delta y'^2_{rms}}{\sigma'^2} \leq 0.02, \text{ or } \quad \Delta y'_{rms} \leq \frac{1}{5}\sigma'.$$

The rms-wakefield kick $\Delta y'_{rms}$ is obtained by averaging of $\Delta y'$ and $\Delta y'^2$ over the longitudinal charge distribution (which is assumed here to be Gaussian):

$$\Delta y'_{rms} = \left(\langle \Delta y'^2 \rangle - \langle \Delta y' \rangle^2 \right)^{\frac{1}{2}} = \left(\frac{2-\sqrt{3}}{2\sqrt{3}} \right)^{\frac{1}{2}} \theta_1 = 0.278 \cdot \theta_1.$$

In order to reduce the geometric wakefield the spoiler can be tapered as shown in fig. 3.7.22. For taper angles $\theta_{tap} \ll 1$ the reduction factor is a linear function of θ_{tap} [32]:

$$k_1 = \frac{6\theta_{tap}}{\pi} \approx \frac{12(R-g)}{\pi(L_{tot}-L_{sp})}. \tag{3.7.4}$$

Of course the beam spoilers are not perfect conductors and for narrow gaps the resistive losses act back on the bunch. The so called resistive wall wakefield kick can be estimated by [33]:

$$\Delta y'(z) = \theta_2 \frac{1}{\sqrt{2\pi}} \int_{s=0}^{\infty} \frac{ds}{\sqrt{s}} \exp\left(-\frac{(z-s)^2}{2} \right); \qquad \theta_2 = \frac{\pi^2 r_e N_B L_{sp}}{2\gamma} \sqrt{\frac{\lambda_{sp}}{\pi \sigma_z}} \frac{\langle \Delta y \rangle}{g^3}, \tag{3.7.5}$$

where L_{sp} is the length of the spoiler and λ_{sp} is a characteristic length calculated from the conductivity σ_{sp} of the spoiler material:

$$\lambda = \frac{1}{c\mu_0\sigma_{sp}}.$$

	$\gamma\varepsilon$ [mm mrad]	β [m]	σ [μm]	σ' [nrad]	g [mm]	g/σ
X:	14	868	158	181	1.3	8
Y:	0.25	6797	59	8.7	1.9	32

Table 3.7.9: *Some beam related parameters at the spoiler locations.*

Here the rms-kick is given by [28]

$$\Delta y'_{rms} = \left(\frac{K(\sqrt{3}/2)}{2\sqrt{\pi}} - \frac{\Gamma^2(1/4)}{8\pi} \right)^{\frac{1}{2}} \cdot \theta_2 = 0.292 \cdot \theta_2.$$

Tapering increases the length of the spoiler and therefore the resistive wall kick. The increase can be estimated by replacing the factor $\sqrt{\lambda_{sp}} L_{sp}/g^3$ in (3.7.5) by an integral over the total length:

$$\frac{\sqrt{\lambda_{sp}} L_{sp}}{g^3} \approx \int_{l=0}^{L_{tot}} \frac{\sqrt{\lambda(l)}}{g^3(l)}\, dl.$$

Thereby we obtain an enlargement factor for the rms-resistive wall wakefield kick of the tapered spoiler of (see geometry in fig. 3.7.22)

$$k_2 = 1 + \frac{1}{2} \sqrt{\frac{\lambda_{tap}}{\lambda_{sp}}} \left(\frac{L_{tot}}{L_{sp}} - 1 \right) \left(1 + \frac{g}{R} \right) \frac{g}{R}. \tag{3.7.6}$$

Here λ_{tap} is the characteristic length of the taper material which could be a thin copper foil for instance. Note that the heating of the taper material is not critical since the beam spot is enlarged by $1/\theta_{tap}$.

As long as the resistive wall wakefield kick is smaller than the geometric wakefield kick, tapering of the spoiler is helpful. The optimum total length of the tapered spoiler L_{tot} is achieved when both kicks have equal strength:

$$0.278 \cdot k_1(L_{tot}) \cdot \theta_1 = 0.292 \cdot k_2(L_{tot}) \cdot \theta_2.$$

Now we can apply these formulas to the TESLA parameters. We consider three possible layouts for the spoiler - a spoiler made of pyrolytic graphite, the graphite spoiler with copper coating and a spoiler made of titanium. For all kinds of spoilers we assume a thickness of 2 radiation lengths and a radius of the beam-pipe of $R = 12.5$ mm. TESLA parameters relevant for the beam spoilers are given in table 3.7.9, material parameters in table 3.7.10 and results for the different layouts in table 3.7.11. It turns out that the graphite spoiler, even untapered, misses the goal of $\Delta y'_{rms} \leq \sigma'/5$ already due to the resistive wall effect (see table 3.7.11). So tapering will not improve the situation in that case. However, the Ti spoiler is uncritical if one applies some tapering. If coating of the inner surface of the graphite spoiler with a thin layer of copper or another material with high electrical conductivity is possible, also such a design could be used.

The conclusion from these considerations is that mechanical collimation of the TESLA beam at amplitudes of $8\sigma_x$ and $32\sigma_y$ can be realized with a tapered Ti spoiler.

	$C_\perp$	$C_\parallel$	Ti	Cu	Au
λ [m]	$2.65 \cdot 10^{-6}$	$1.06 \cdot 10^{-8}$	$1.47 \cdot 10^{-9}$	$4.5 \cdot 10^{-11}$	$6.1 \cdot 10^{-11}$

Table 3.7.10: *Characteristic length of several materials. Note the anisotropic properties of pyrolytic graphite. We assume that the material is aligned along the beam in the direction of the higher conductivity.*

	geometric		resistive wall		opt. tapered		opt. len. [m]	
	$\frac{\sigma'_x}{\Delta x'_{rms}}$	$\frac{\sigma'_y}{\Delta y'_{rms}}$	$\frac{\sigma'_x}{\Delta x'_{rms}}$	$\frac{\sigma'_y}{\Delta y'_{rms}}$	$\frac{\sigma'_x}{\Delta x'_{rms}}$	$\frac{\sigma'_y}{\Delta y'_{rms}}$	L^x_{tot}	L^y_{tot}
C	9.0	1.7	9.4	4.0	-	-	-	-
C,Cu	9.0	1.7	142.1	60.7	130.2	48.1	1.0	1.5
Ti	9.0	1.7	132.8	56.7	122.8	45.9	0.66	1.2

Table 3.7.11: *Wakefield kicks for different spoiler materials and taperings for a beam offset of 1 σ. The table contains the geometric and resistive wall kicks for the untapered spoiler and the geometric kicks for an optimal tapered spoiler. Given is always the value of $\sigma'/\Delta y'_{rms}$ which should be larger than 5 for a luminosity reduction of less than 2%. Furthermore the total length for an optimal tapered spoiler is given.*

Emittance growth from wakefields is practically negligible in that case. A graphite spoiler would be advantageous in view of its thermal properties, provided that the problem of coating with highly conductive material can be solved.

3.7.9 Beam Extraction and Dump

3.7.9.1 Extraction Beamline

After passing through the electrostatic/magnetic separator adjacent to the FD, the separation of the outgoing beam from the incoming beam is enhanced by septum magnets in order to stay clear from the next beamline elements of the FFS (see fig. 3.7.23).

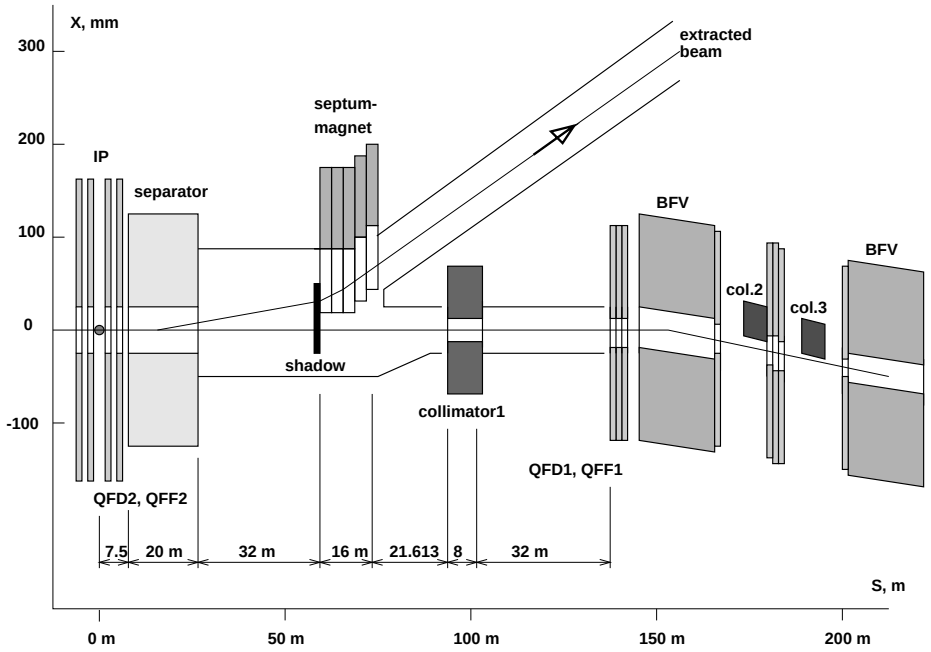

Figure 3.7.23: *Layout of the beam extraction system after the IP.*

A low-field design ($\approx$ 0.1 T) for the septum is chosen to allow for a thin septum bar. This helps to reduce the heat load from beamstrahlung and tails of the disrupted beam. The septum is shielded by a watercooled screen as sketched in fig. 3.7.24. The distribution of the heat load has been calculated using computer simulations of the beam-beam interaction and electromagnetic shower simulations in the screen, see fig. 3.7.25. After the septum, the positron beam is guided to the beam dump whereas the electron beam is captured in a special beam optical system, as described in section 3.4.5. The transfer line to the dump does not require any focussing elements, but a horizontal and vertical deflection of 10 mrad each are foreseen to increase the separation from the incoming beam and to have the muon beam emerging from the dump going downwards, away from the surface. The synchrotron radiation in these dipole magnets is sufficient to blow up the beamsize to about $2\,mm^2$ if the dump is placed 250 m away from the IP. Thus damage to the beamdump window and to the absorber block is excluded (see the following section), even for the case of an "unspoiled" beam which has not experienced the beam-beam interaction.

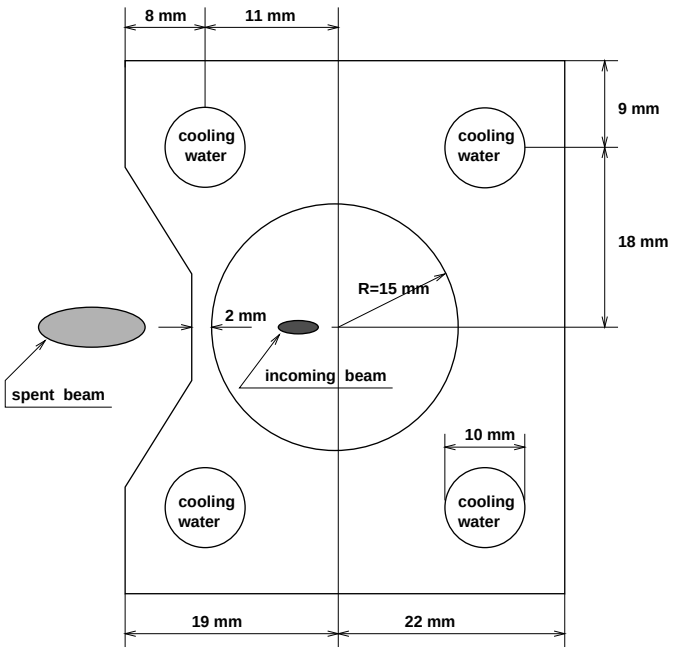

Figure 3.7.24: *Cross section of the septum magnet screen which absorbs losses from beamstrahlung and spent beam tails.*

3.7.9.2 Beam Dump

This section focusses on the question how to dispose of both the electron- as well as the positron beam after the collision. Based on shower, heat transfer and mechanical stress calculations a beam dump design capable of handling the $250\,GeV$ beams in TESLA is presented. After introducing the requirements on such a beam dump simple estimations on energy deposition and heat transfer answer the question of adequate absorber materials. Using shower simulation codes a beam absorber is calculated in more detail with respect to absorption efficiency and local energy densities the latter one giving a lower limit for the effective beam size when entering the absorber. The problem of induced radioactivity (production and handling of long lived isotopes) is mentioned very briefly, since the whole complex of radiation safety is discussed separately in section 3.11.

Requirements

The energy E_t carried in one bunchtrain, i.e. macropulse, is $1.6\,MJ$ for the TESLA scheme. This would suffice to melt $2.2\,kg$ of iron, $2.8\,kg$ of aluminium, $4.1\,kg$ of copper or $40\,kg$ of lead. Although being rather high, solutions exist to handle macropulse energies of that amount, e.g. at the proton machine of HERA, where the beam dump is capable of absorbing a complete fill, i.e. $820\,GeV$ protons with a total energy of $2.6\,MJ$ in a train of $20\,\mu s$, but this repeats typically less than one time in 8 hours only. Contrary to that the linear collider operates with high repetition rate, leading

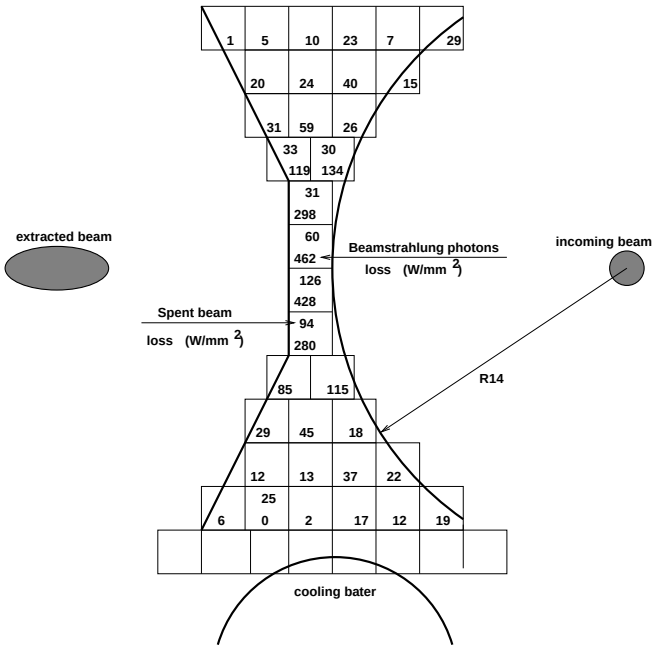

Figure 3.7.25: *Power distribution on the face of the septum screen from spent beam losses and beamstrahlung. In a 1 m long screen the temperature rise in steady state operation remains below 20 K (most of the produced shower particles are scattered out to the sides).*

to an enormous average beam power of about 8 MW. This represents not only a huge heat load, but is also a source of high radiation and isotope production. In addition to the thermal capabilities the integral radiation leakage should not exceed 1 % of the incident beam power, which is still 80 kW. Of course the shielding around the dump will take some fraction of it and the contribution from the leaking particles to the total activation is less than 1 % because of their low energy.

The decision on the location of the beam dump depends strongly on its size. From the point of view of civil engineering costs and simplicity a solution of putting the absorber inside the tunnel is preferred instead of building an extra hall for it. On the other hand, additional shielding around the tunnel would be required to avoid activation of ground water. The final layout for the dump region still needs to be worked out.

Assuming the absorber would fit into the tunnel figure 3.7.26 illustrates a very schematic top view of the area between interaction point (IP) and beam dump. From the point of view of radiation and induced radioactivity there is no strong argument to put the beam dump outside if it would fit inside, since there will be already an area of higher dose rate level in the vicinity of the IP due to the presence of two collimation systems, that can not be avoided there. Getting different deflection in the separation region the low energy tail of the disrupted beam can not be transported through the beamline towards the dump. Distributed collimators have to scrape this fraction of the beam (see also section 3.4.5), which is between 10 % and 20 % of the total

intensity corresponding to a power in the order of $1\,MW$. In addition beamstrahlung in the order of $200\,kW$ coming from the IP must not hit components of the incoming beamline. Therefore it is equipped with beamstrahlung collimators.

Besides the absorber for the spent beam there need to be a possibility to dispose of the beam when not passing through the IP but being extracted after the main linac during its commissioning. If it is designed symmetrically the same absorber could be used for both purposes being hit either by the spent beam or the commissioning beam from opposite sides, but excluding simultaneous operation because of power reasons. Since this would not allow independent commissioning of one main linac while the other beam passes through the IP, two beam dumps with identical specification have to be put behind each other as indicated in figure 3.7.26 on either side of the IP. The commissioning dump will also be a part of an emergency dump system. Whenever the beam tends to get lost in the collimation system behind the main linac, which protects the experimental area, the particle source at the injector has to be switched off and the beam which is still in the main linac will be deflected onto this dump using fast extraction kickers at the end of the main linac.

Apart from these main dumps there have to be additional beam absorbers in the whole complex of the linear collider facility, e.g. at the FEL laboratory. Nevertheless the requirements on the main dump are the most severe ones. Having found a feasible concept for the main dump will automatically give a solution for the other dumps. From the previous discussion the requirements on such a main dump can be summarized as follows:

1. Withstand absorption of $1.6\,MJ$ energy pulses in combination with $8\,MW$ average power
2. Energy absorption efficiency $\geq 99\,\%$
3. Compact as possible to be put inside the tunnel
4. Production rate of dangerous and long lived isotopes as small as possible

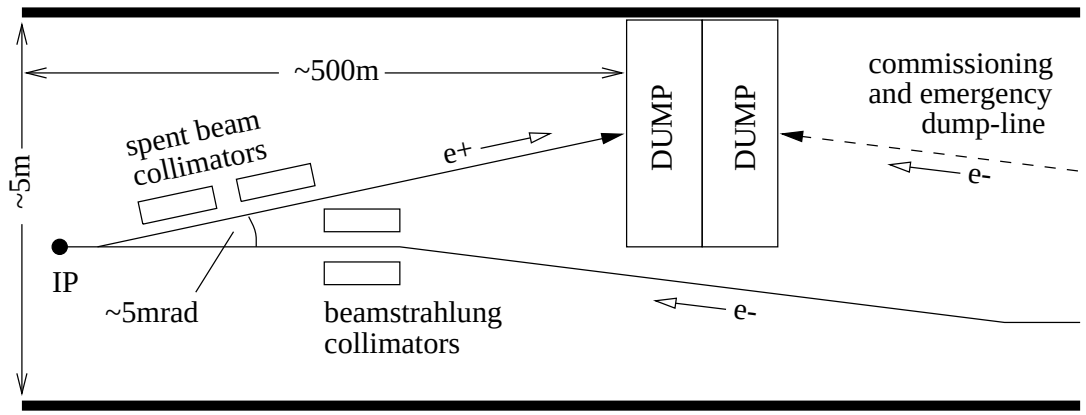

Figure 3.7.26: *Schematic topview of the area between IP and dump assuming the absorber fits inside the tunnel.*

5. Sufficient shielding to prevent groundwater and soil from being activated

Electromagnetic Showers

When hitting the absorber a high energy electron or positron beam initiates an electromagnetic shower (EMS), consisting of electrons, positrons and photons. In addition high energy photons can produce hadrons by means of photonuclear reactions. This is of major interest for the estimation of induced radioactivity, but less important for considerations on energy deposition since this is dominated by ionisation and exitation of atoms due to charged EMS components.

With respect to a cylindrical coordinate system an electron of energy E_0 enters a homogeneous material at $r = z = 0$ in positive z-direction. At first the combination of bremsstrahlung and pair production happening in average once in every radiation length for every electron, positron or photon leads to an exponential growth of the number of particles with z. Since the energy of the secondaries reduces similarly, this process stops when particles have reached the critical energy E_c, where ionisation reactions become dominant. The corresponding longitudinal position $z = t_{max}$ is called the shower maximum. That is where the longitudinal energy density defined as:

$$dE/dz = \int_{r=0}^{\infty} \int_{\phi=0}^{2\pi} dE/dV \; r \, d\phi \, dz$$

has its maximum value. Since this integration depends on the radial shower distribution it is obvious, that for a given material the maximum local energy density $(dE/dV)_{max} = \rho \cdot (dE/dm)_{max}$ appears at a position that depends on the incoming beamsize, while t_{max} is independent of it. With the radiation length X_0 and the critical energy E_c of a given material the development of the shower can be parametrized. Therefore the position of the shower maximum t_{max} and the particle multiplicity $M(t_{max})$ at that point can be expressed as [34]:

$$\begin{aligned} t_{max}(E_0) &= 1.01 \cdot \left(ln(\tfrac{E_0}{E_c}) - 1 \right) \cdot X_0 \\ M(t_{max}, E_0) &= 0.31 \cdot \tfrac{E_0}{E_c} \cdot \left(ln(\tfrac{E_0}{E_c}) - 0.37 \right)^{-\frac{1}{2}} \end{aligned} \tag{3.7.7}$$

where E_0 is the energy of the primary electron resp. positron. Assuming that at the shower maximum all the particles are still minimum ionising a rough estimate on the longitudinal energy density $(dE/dz)_{max}$ at the shower maximum created by one primary particle can be given as:

$$(dE/dz)_{max} \approx M(t_{max}, E_0) \cdot (dE/dz)_{min} \tag{3.7.8}$$

where $(dE/dz)_{min}$ is the energy deposited by one minimum ionising particle. The radial size of the shower is characterized by the Molière radius $R_M = 21.2MeV \cdot X_0/E_c$. In order to contain 98 % (1 % energy leakage radially and longitudinally) of the primary energy a cylindrical absorber has to have a radius $R_{99\%}$ and a length $L_{99\%}$ given by [35]:

$$L_{99\%} = \left[1.52 \cdot ln(\tfrac{E_0}{MeV}) - 4.1 \cdot ln(\tfrac{E_c}{MeV}) + 17.6 \right] \cdot X_0 \quad \text{and} \quad R_{99\%} \approx 5 \cdot R_M$$

		C	Al	Fe	Cu	Pb	H_2O
$X_0\ [cm]$		25.1	8.89	1.76	1.44	0.56	36.1
$R_M\ [cm]$		7.01	4.71	1.78	1.62	1.56	9.53
$E_c\ [MeV]$		75.9	40.0	21.0	18.8	7.6	80.3
$(dE/dz)_{min}\ [MeV/cm]$		3.03	4.37	11.6	12.9	11.7	2.03
$L_{99\%}\ [cm]$		470	190	42	35	16	670
$R_{99\%}\ [cm]$		35	24	8.9	8.1	7.8	48
$\rho\ [g/cm^3]$		1.7	2.7	7.87	8.96	11.35	1.0
$m\ [kg]$		3080	930	82	65	35	4850
$t_{max}\ [cm]$	from eq. 3.7.7	180	69	15	12	5.3	257
	MARS	200	80		14		260
$(\frac{dE}{dz})_{max}\ [\frac{GeV}{cm}\ per\ e]$	from eq. 3.7.7	1.11	2.93	14.3	17.6	37.7	0.707
	MARS	1.1	2.8		16.8		0.8

Table 3.7.12: *Basic properties of an electromagnetic shower initiated by a primary particle of energy $E_0 = 250\,GeV$ in different materials.*

From the given expressions most of the basic properties of the shower can be estimated. They are listed in table 3.7.12 for most likely absorber materials, where t_{max} and $(dE/dz)_{max}$ are compared with the result of the simulation code MARS, which has been developed over many years at IHEP (Protvino, Russia) and FNAL (Batavia, USA). As for calculating the maximum steady state temperature level, which is determined by $(dE/dz)_{max}$ a simulation code is not required since the calculated result agrees within 15 %. But when dealing with local energy densities dE/dm, designing a composite absorber or including hadronic effects the simulation can not be avoided. In addition to the shower size for 98 % energy containment the mass $m = \rho \cdot \pi \cdot R^2_{99\%} \cdot L_{99\%}$ of a corresponding absorber is given as well. Absorbers of that size would take 98 % of the shower but whether they withstand heating due to local energy densities and average power is subject to the following section 3.7.9.2. This is easy to judge in the case of the Pb absorber. With a mass of $35\,kg$ only it will be completely melted by the energy of one bunchtrain. It has to be mentioned, that the graphite parameters are valid for a material coming from a pyrolytic production process. Therefore the density is 75.9 % of the theoretical value only. As a consequence the radiation length is increased and the minimum ionisation loss is decreased by the same factor.

Basic Considerations on Heating and Choice of Material

The incident particle leads to a certain distribution of deposited energy with a maximum local energy density $(dE/dm)_{max}$ somewhere on the shower axis. Even during the long passage time $T_t = 800\,\mu s$ of a bunchtrain, heat conduction is negligible since the diffusion length $< d >$ given by:

$$< d >= \sqrt{\frac{\lambda \cdot T_t}{\rho \cdot c}} \quad \text{with} \quad \lambda := \text{heat conductivity} \quad c := \text{specific heat}$$

is only $0.3\,mm$ for copper or $0.26\,mm$ for graphite, which is small compared to the radial shower size respectively the required beamsize at the dump entrance as will be seen later. Therefore the instantaneous temperature rise ΔT_{inst} is directly proportional to the density of the deposited energy. Its maximum value $(\Delta T_{inst})_{max}$ is given by:

$$N_t \cdot (dE/dm)_{max} = \int_{T_0}^{T_0+(\Delta T_{inst})_{max}} c(T)\,dT \tag{3.7.9}$$

where T_0 is the temperature just before the passage of the bunchtrain. The integral form takes a temperature dependent specific heat $c(T)$ into account, which is quite important in the case of graphite, where it can be described using the following fit function:

$$c(T) = 1.48 \cdot \tfrac{J}{g \cdot K} \cdot (1.44 - e^{-\frac{T}{511\,^\circ C}}) \quad \text{with T in degree celcius}$$

After the passage of the bunchtrain this temperature on the shower axis decays until the next bunchtrain arrives. Therefore the temperature varies with time in a sawtooth-like manner. On the other hand for a continuous beam with the same average power as for the pulsed one an equilibrium temperature drop ΔT_{eq} is expected between the shower axis and the cooled edge.

Let us first deal with the equilibrium situation, i.e. how to get rid of the average beam power. For all solids besides their heat conductivity this problem is determined by the area and the thickness through which the heat has to flow. We assume that the beam is evenly distributed along a circle with radius r_1 on the face of a cylindrical dump. In order to contain the shower radially the outer radius r_2 has to be $r_2 = r_1 + R_{99\%}$. Assuming that all the deposited energy flows radially from r_1 to r_2 the temperature drop $(\Delta T_{eq})_{max}$ between both radii at the position of the shower maximum can be given as:

$$(\Delta T_{eq})_{max} = (\tfrac{dP}{dz})_{max} \cdot \tfrac{1}{2\pi\lambda} \cdot ln(r_2/r_1) \quad \text{with} \quad (\tfrac{dP}{dz})_{max} = \tfrac{I_{ave}}{e} \cdot (\tfrac{dE}{dz})_{max} \tag{3.7.10}$$

For each material of interest we set a maximum allowed temperature difference ΔT_{max}, either given by its plasticity limit $\sigma_{0.2}$ or by 20 % of its melting temperature T_{melt}, depending which of both represents the lower limit, i.e.:

$$\Delta T_{max} \approx \text{Min}\,[\sigma_{0.2}/(E \cdot \alpha) \text{ or } 0.2 \cdot (T_{melt} - 20^\circ C)]$$

where E is the elastic modulus and α the coefficient of linear thermal expansion.

For an average beamcurrent $I_{ave} = 32\,\mu A$, the power density at the shower maximum $(dP/dz)_{max}$ was derived from the calculated values of $(dE/dz)_{max}$ according to equation 3.7.8 as listed in table 3.7.12. They vary between $36\,kW/cm$ (C) and $1.2\,MW/cm$ (Pb). From these values the required radius $r_1 = r_2 - R_{99\%}$ and the resulting outer diameter of a dump $D = 2 \cdot (r_1 + R_{99\%})$ in order to keep $(\Delta T_{eq})_{max} \leq \Delta T_{max}$ can be calculated according to equation 3.7.10. The results are listed in table 3.7.13. Except for graphite the diameter of all other materials exceeding several $10\,m$ excludes their installation inside the tunnel and is even far off from a reasonable limit to be built

	C	Al	Fe	Cu	Pb
$(dP/dz)_{max}$ $[kW/cm]$	36	94	458	560	1200
λ $[W/(cm \cdot K)]$	1.6	2.0	0.8	3.8	0.35
ΔT_{max} $[K]$	800	60	240	150	30
r_1 $[m]$	1.4	30	34	13	1400
$D = 2 \cdot (r_1 + R_{99\%})$ $[m]$	3.5	60	68	26	2800

Table 3.7.13: *Minimum required diameter D of a dump in order to keep the maximum equilibrium temperature drop $(\Delta T_{eq})_{max} \leq \Delta T_{max}$ for $E_0 = 250\,GeV$ and $I_{ave} = 32\,\mu A$.*

anyhow. On the one hand graphite has a high radiation length leading to moderate power densities. On the other hand its excellent thermomechanical properties allow a high working temperature around $800°C$ not determined by the plasticity limit as it is for the other materials. In addition there is no safety problem in handling and machining graphite and its relatively low mass number limits the variety of produced isotopes. This all makes graphite the best candidate for a dump built from a solid material. When estimating the diameter of the solid cylindrical dump only cooling at the outer surface at $r_1 + R_{99\%}$ was assumed. Since r_1 is large enough additional cooling at an inner surface at $r_1 - R_{99\%}$ is possible. This will either reduce the equilibrium temperature or it allows to decrease the radial size. Nevertheless a graphite based absorber will have an outer diameter between $2\,m$ and $3\,m$ determined by heat conduction not shower containment and a length given by $L_{99\%}$ of about $5\,m$.

This is completely different for a liquid absorber such as water. Having even a little higher radiation length than graphite it is also a good candidate for a dump design. With $23\,kW/cm$ the maximum power density is not significantly less than in graphite, but instead of distributing the beam across the absorber in order to increase the area for heat conduction, one can introduce a sufficiently high water flow transversely to the shower axis, so that the water in the core of the shower is exchanged within the repetition time of bunchtrains. Under these circumstances the average power will be transported to an external heat exchanger and the size of the absorber is purely determined by the 99 % shower containment constraint. This will give a diameter of $2 \cdot R_{99\%} \approx 1\,m$ and a length of $L_{99\%} \approx 7\,m$ in the case of water. Being at least a factor of 2 more compact radially the length is only 40 % increased with respect to a graphite absorber. Although this is advantageous there are qualitative differences that will be discussed at the end of this section.

Now we have to consider the implications due to instantaneous heating during the passage of one bunchtrain. As described in equation 3.7.9 the maximum temperature rise $(\Delta T_{inst})_{max}$ depends on the number of particles N_t in a bunchtrain and the maximum local energy density in the shower $(dE/dm)_{max}$ deposited by one particle. For a given material only the size of the incident beam can be varied in order to reduce the local energy density and thus the instantaneous heating. Assuming a $250\,GeV$ gaussian beam with an aspect ratio of 1:1 the maximum local energy density $(dE/dm)_{max}$ and its longitudinal location on the shower axis was calculated for graphite and water

Graphite								
$\sigma_x = \sigma_y$ $[mm]$	0.1	0.5	1	2	3	5	7.5	10
$(dE/dm)_{max}$ $[GeV/g\ per\ e]$	13	2.8	1.1	0.45	0.27	0.13	0.07	0.05
z-position of $(dE/dm)_{max}$ $[cm]$	50	80	100	125	130	150	165	175

Water						
$\sigma_x = \sigma_y$ $[mm]$	1	3	5	10	30	50
$(dE/dm)_{max}$ $[GeV/g\ per\ e]$	1.05	0.25	0.12	0.05	0.009	0.004
z-position of $(dE/dm)_{max}$ $[cm]$	145	190	205	220	230	250

Table 3.7.14: *Maximum local energy density normalized to one primary particle in a graphite or water absorber deposited by a* $250\,GeV$ *beam as a function of its transverse beamsize.*

as a function of the transverse beamsize $\sigma_x = \sigma_y$ by means of the shower simulation code MARS. From these results as listed in table 3.7.14 a lower limit for the required beamsize at the dump entrance can be given. Due to steady state heating the temperature T_0 before the passage of a bunchtrain will be about $400°C$ in a graphite based dump (see next section). The remaining margin up to the working temperature limit of $800°C$ can be allowed for instantaneous heating. Taking into account the temperature dependent specific heat of graphite the corresponding difference in enthalpy per mass unit is $660\,J/g$ for $T_0 = 400°C$ and $(\Delta T_{inst})_{max} = 400\,K$. For a bunchtrain with $N_t = 4 \cdot 10^{13}$ this requires a $(dE/dm)_{max}$ of less than $0.1\,GeV/g\ per\ e$ corresponding to a beam size with $\sigma_x = \sigma_y$ not less than about $6\,mm$.

In the case of water $T_0 = 40°C$ and $(\Delta T_{inst})_{max} = 40\,K$ are reasonable assumptions in order to prevent it from boiling. Therefore about $170\,J/g$ can be used for instantaneous heating. From the same considerations as above the relevant limits are $0.027\,GeV/g\ per\ e$ and $\sigma_x = \sigma_y \approx 20\,mm$. The estimates on the required beamsize have to be regarded as lower limits for an effective spotsize over which the particles of one bunchtrain have to be distributed at the dump entrance. In most cases being rather large this spotsize is not automatically achieved by the betafunction and the emittance of the beam at the position of the dump. Additional measures such as a defocussing quadrupole, a thin foil for spoiling the emittance, a fast sweeping system which distributes the beam within the time T_t of one bunchtrain passage or any combination of it have to be taken. From this point of view a water absorber requires more effort.

As proven in this section even for the high average power of $8\,MW$ an edge cooled solid dump made from graphite is possible. Water can be used as an alternative as proposed for the NLC [36]. On the one hand a water absorber is more compact and due to the main contribution from short lived isotopes the dose rate in $1\,m$ distance after $1\,year$ of $8\,MW$ operation decays rather rapidly within a waiting time of $3\,hours$ down to a level of $20 - 30\,mSv/h$ ($1\,Sv = 100\,rem$), which can be reduced by a shielding factor of 10^2 with $5\,cm$ of lead [37]. The corresponding dose rate for a graphite absorber is around $70\,mSv/h$, i.e. only a factor of 2 higher. This would allow access

or at least walking by at the dump region. The remaining dose rate is determined by $^7Be\,(t_{1/2} = 54\,days)$ but can be removed in a resin filter. On the other hand there are severe safety problems correlated with a water absorber. Having an annual production rate of $11.4\,Ci/MW$ the activity of tritium ($t_{1/2} = 12\,years$) after 1 year of $8\,MW$ operation is $88\,Ci$ equivalent to $33\,cm^3$ of $^3H_2$ gas. Since distributed in the whole system of water cooling special care has to be taken to prevent leaking of it. There is no conclusive approach how to handle the tritium. Dilution of course is a bad idea. The presently allowed concentration of $800\,\mu Ci/m^3$ which can be put into waste water would require $3.5\,l/s$ continous exchange of the absorberwater with fresh water. Another safety problem arises from the radiolysis of water. Due to a production rate of $0.3\,l/s$ per MW deposited beam power [38], $2.4\,l/s$ hydrogen is produced at $8\,MW$ operation, which can be recombined to H_2O catalytically. Again any leakage of the system has to be avoided because a concentration of 4 % H_2 in air is explosive. Being proportional to the directly deposited beam power all the water related problems are less by a factor of 100 for the cooling circuit of an edge cooled graphite dump. Although the amount of ^{3}H production will not be significantly different in graphite, it will like all other produced isotopes be bounded and localized inside the solid and not spread around in a fluid with the danger of getting lost by leakage. For this qualitative difference the graphite based solution is preferred. An optimized design using shower simulations is presented in the following section. The solution using water can be regarded as a backup.

Absorber Design Based on a Graphite Core

From considerations in the previous section we know that the graphite absorber has to look like a hollow cylinder with a radial thickness of Δr between an inner resp. outer radius of $r_1 \pm \Delta r/2$, while the beam is distributed along a circle with radius r_1 at the face of this dump. Putting a material of higher density and better thermal conductivity in the region of the transverse shower tails, where it can survive, will reduce both Δr and r_1. Longitudinally the dump is not sectioned. Several runs of MARS simulations were made to optimize this layout. The result is shown in figure 3.7.27. A graphite tube with $r_1 = 1\,m$ and a radial thickness of $10\,cm$ is embedded between an inner and outer radial layer of aluminium $10\,cm$ thick each. For its smaller radiation length (see table 3.7.12) only $5\,cm$ of copper can be used alternatively. This compound has a total radial thickness of $\Delta r = 30\,cm$ with Al respectively $\Delta r = 20\,cm$ with Cu, an outer diameter D of $2.3\,m$ resp. $2.2\,m$, a total mass of $27\,tons$ resp. $40\,tons$ and will be cooled at the inner and outer surface at $r_1 \pm \Delta r/2$. A total length of $L = 6\,m$ guarantees 99 % absorption of the primary energy in both cases.

Distribution of the beam along a circle with radius $r_1 = 1\,m$ can be achieved by means of an orthogonal pair of dipoles harmonically excited at the same frequency but shifted in phase by 90°. If placed $100\,m$ upstream from the dump the maximum deflecting angle of each magnet has to be $10\,mrad$, which requires an integrated field-strength of about $9\,Tm$ for a $250\,GeV/c$ beam. To provide a homogeneous azimuthal heat source the oscillation period of this slow sweeping system has to be significantly

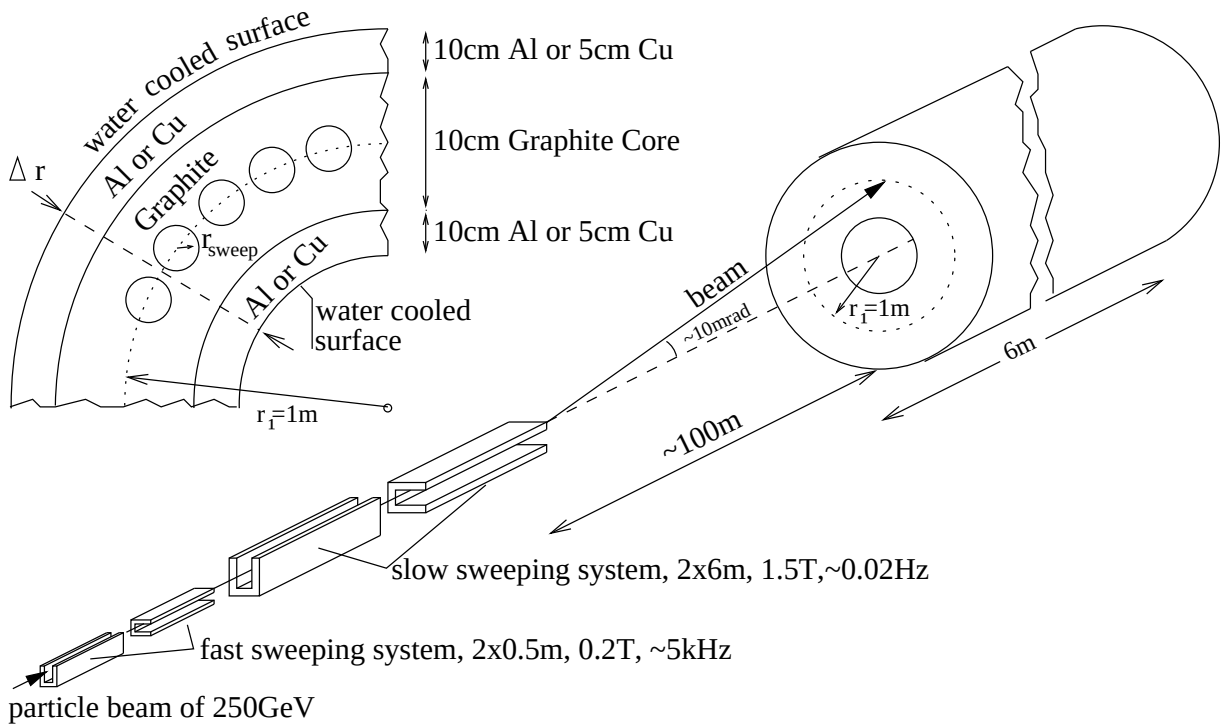

Figure 3.7.27: *Dump scheme based on a solid absorber with a graphite core.*

conduction in C between $100cm \le r \le 105cm$	transfer C → Al or Cu at $r = 105cm$	conduction in Al between $105cm \le r \le 115cm$	conduction in Cu between $105cm \le r \le 110cm$	transfer Cu or Al → H_2O at $r = 105$ or $110cm$
$190\,K$	$\approx 50\,K$	$135\,K$	$45\,K$	$\approx 50\,K$

Table 3.7.15: *Contributions to the equilibrium temperature rise due to heat conduction or heat transfer in the C-Al or C-Cu composite dump at the shower maximum for* $E_0 = 250\,GeV$ *and* $I_{ave} = 32\,\mu A$.

faster than thermal diffusion processes. Since the thermal time constant for this dump scheme is around $200\,s$ the frequency of the slow sweepers should be $1/50\,Hz$ or more.

The resulting equilibrium temperature rise at the shower maximum ($t_{max}(\mathrm{C}) \approx 2\,m$) for a $250\,GeV$ beam with $I_{ave} = 32\,\mu A$ is listed in table 3.7.15. The maximum heat flux at the water cooling boundary is roughly $27\,W/cm^2$. The temperature will rise by about $50\,K$ according to a typical heat transfer coefficient of $0.6\,\frac{W}{cm^2 \cdot K}$ for water at metallic walls. The graphite metal boundary is more crucial, because specific heat transfer is only about $0.2\,\frac{W}{cm^2 \cdot K}$ [39]. The effective surface has to be increased at least by a factor of 2, which was already taken into account when estimating a ΔT of $50\,K$ across this boundary. The technical design has to guarantee that the thermal contact of this boundary is not lost due to different expansion during warm up or cool down of the dump. Including the temperature drops from heat conduction and assuming

a temperature of $50°C$ for the cooling water, the graphite core at $r = 1\,m$ rises up to a temperature of $475°C$ when neighboured by aluminium. For its better thermal conductivity this temperature can be reduced to $385°C$ when using copper.

The following considerations on instantaneous heating are based on a beamsize with $\sigma_x = 3\,mm$ and $\sigma_y = 0.5\,mm$ at the dump entrance for a beam having not interacted (according to the preceding section the minimum beam cross section is $2\,mm^2$). From table 3.7.14 we know already that a minimum effective spotsize of $\sigma_x \cdot \sigma_y = 36\,mm^2$ is required in order to keep $(\Delta T_{inst})_{max} \leq 400\,K$. Therefore the above given beamsize is not large enough. A fast sweeping deflection system is proposed to increase the effective spotsize. Similar to the slow sweeping system it consists of a pair of orthogonal kicker magnets, again oscillating with a phase shift of 90°. It has to distribute the particles of one bunchtrain along a small circle with radius r_{sweep} within the bunchtrain passage time $T_t = 800\,\mu s$. Therefore the frequency of the fast sweeping system needs to be a few kHz. Table 3.7.16 gives the maximum local energy density $(dE/dm)_{max}$ normalized to one primary particle as a function of r_{sweep}. In order to

$r_{sweep}\ [mm]$	0	3	5	10	20
$(dE/dm)_{max}\ [GeV/cm\ per\ e]$	0.63	0.32	0.12	0.06	0.032

Table 3.7.16: *Maximum local energy density in graphite as a function of the sweep radius of the fast deflection system based on an incident beamsize with* $\sigma_x = 3\,mm$ *and* $\sigma_y = 0.5\,mm$.

keep $(\Delta T_{inst})_{max} \leq 400\,K$ less than $0.1\,GeV/cm\ per\ e$ and thus $r_{sweep} \approx 10\,mm$ is required. Located in the neighbourhood of the slow sweeping system a deflection angle of $0.1\,mrad$ is needed. The main parameters of the slow and fast deflection systems are summarized in table 3.7.17. The instantaneous temperature rise in the Al or Cu

	magnetic field in deflector	length of deflector	frequency $[Hz]$
slow deflection system	$1.5\,T$	$2 \times 6\,m$	$\geq 0.02\,Hz$
fast deflection system	$0.2\,T$	$2 \times 0.5\,m$	$\approx 5\,kHz$

Table 3.7.17: *Main parameter of both sweeping systems for a* $250\,GeV$ *beam.*

material is only about $20\,K$.

With this scheme the maximum temperature in graphite is kept below a maximum reasonable working temperature of $800°C$. As a consequence of the slow deflection system a large beampipe and if not directly flanged onto the dump a huge exit window is required. The angle of $10\,mrad$ needs to be taken into account by shaping the dump conically rather than cylindrically.

Bibliography

[1] Murray J.J., K.L. Brown and T. Fieguth, *The Completed Design of the SLC Final Focus System*, Proc.of Part. Acc. Conf., Washington, D.C., March 1987 and SLAC-PUB–4219 (Feb.1987).

[2] D. Burke for the FFTB Collaboration, *Results from the Final Focus Test Beam*, Proc. of the IVth European Particle Accelerator Conf., London 1994, Vol. I, p. 23.

[3] Rifflet J.M. et al., *Cryogenic and Mechanical Measurements of the first two LHC Lattice Quadrupoles Prototypes*, EPAC94 Conf., London, Great Britain, 1994.

[4] Grote H. and F.C. Iselin, *The MAD Program*, CERN/SL/90-13 (AP) Rev.3 (Jan.1993).

[5] B. Baklakov, P. Lebedev, V. Parkhomchuk, A. Sery, A. Sleptsov, V. Shiltsev, INP 91-15; Tech. Ph. **38**, 894, (1993).

[6] V. Juravlev, A. Sery, A. Sleptsov, W. Coosemans, G. Ramseier, I. Wilson, CERN SL/93-53, CLIC-Note 217, 1993.

[7] V. Juravlev, P. Lunev, A. Sery, A. Sleptsov, K. Honkavaara, R. Orava, E. Pietarinen, *Seismic Conditions in Finland and Stability Requirements for the Future Linear Collider*, HU-SEFT R 1995-01, Helsinki 1995.

[8] V. Shiltsev, B. Baklakov, P. Lebedev, J. Rossbach, C. Montag, *Measurement of Ground Vibrations and Orbit Motion at HERA*, DESY HERA 95-06, June 1995.

[9] Shigeru Takeda, K. Kudo, A. Akiyama, Y. Takeuchi, T. Katoh, Y. Kanazawa, S. Suzuki, *Slow Ground Motion and Large Future Accelerator*, Proc. EPAC 96, 1996.

[10] C. Adolphsen, G. Mazaheri, T. Slaton, in: Proc. of Workshop on Physics and Experiments with Linear Colliders, Tsukuba, 1995.

[11] A. Sery, O. Napoly, Phys. Rev. E. **53**, 5323, (1996).

[12] R. Brinkmann, J. Rossbach, *Observation of Orbit Motion in HERA Covering Eight Decades in Frequency*, Nucl.Instr.Meth.A **350**, 8, (1994).

[13] V. Shiltsev, *Space-Time Ground Diffusion: the ATL Law for Accelerators*, Proc. of Workshop on Accelerator Alignment, Tsukuba, 1995.

[14] R. Pitthan, *Re-Alignment: It is the Tunnel Floor which Moves, Isn't it?*, SLAC-PUB 95-7043, 1995.

[15] A. Sery, A. Mosnier, DAPNIA/SEA/96-06, CEA Saclay, 1996.

[16] C. Montag,*Active Stabilisation of Quadrupole Vibrations for Linear Colliders*, DESY 96-053, 1996.

[17] A. Sery,*Ground Motion Studies with Respect to Linac Performance*, Proc. of the Linac 96 Conference, Geneve 1996.

[18] P. Tenenbaum, D. Burke, S. Hartman, R. Helm, J. Irwin, R. Iverson, P. Raimondi, W. Spence, V. Bharadwaj, M. Halling, J. Holt, J. Buon, J. Jeanjean, F. Le Diberder, V. Lepeltier, P. Puzo, K. Oide, T. Shintake, and N. Yamamoto, *Beam Based Optical Tuning of the Final Focus Test Beam*, SLAC-PUB-95-6770, May 1995. 3pp. Presented at 16th IEEE Particle Accelerator Conference (PAC 95) and International Conference on High Energy Accelerators, Dallas, Texas, 1-5 May 1995.

[19] P. Tenenbaum, D. Burke, R. Helm, J. Irwin, P. Raimondi, K. Oide, and K. Flöttmann, *Beam Based Magnetic Alignment of the Final Focus Test Beam*, SLAC-PUB-95-6769, May 1995. 3pp. Presented at 16th IEEE Particle Accelerator Conference (PAC 95) and International Conference on High Energy Accelerators, Dallas, Texas, 1-5 May 1995.)

[20] G. Bowden, P. Holik, S.R. Wagner, G. Heimlinger, and R. Settles, *Precision Magnet Movers for the Final Focus Test Beam*, Nucl. Instrum. Meth.A368:579-592,1996.

[21] P. Emma, J. Irwin, N. Phinney, P. Raimondi, N. Toge, N.J. Walker and V. Ziemann, *Beam Based Alignment of the SLC Final Focus Sextupoles*, SLAC-PUB-6209, May 1993. 3pp. Presented at 1993 Particle Accelerator Conference (PAC 93), Washington, DC, 17-20 May 1993.

[22] N. J. Walker, *Beam Phase Space and Energy Measurements in TESLA and SBLC*, to be published as a TESLA report.

[23] *Zeroth-Order Design Report for the Next Linear Collider*, SLAC Report 474, May 1996.

[24] E. G. Bessonov, J. Pflüger, G.-A. Voss and N. J. Walker, *Beam Size Measurements in a Linear Collider using an X-ray Gradient Undulator*, DESY internal report DESY M 96-18, September 1996.

[25] T. Shintake, K. Oide, N. Yamamoto, A. Hayakawa, Y. Ozaki, D. Burke, R.C. Field, S. Hartman, R. Iverson, P. Tenenbaum, and D. Walz, *Experiments of Nanometer Spot Size Monitor at FFTB using Laser Interferometry*, KEK-PREPRINT-95-46, May 1995. 3pp. Contributed paper at 1995 Particle Accelerator Conference and International Conference on High-Energy Accelerators, May 1 - 5,1995, Dallas, Texas, U.S.A. "Zeroth-Order Design Report for the Next Linear Collider", SLAC Report 474, May 1996.

[26] N.J. Walker, J. Irwin, and M. Woodley, *Global Tuning Knobs for the SLC Final Focus*, SLAC-PUB-6207, Apr 1993. 3pp. Presented at 1993 Particle Accelerator Conference (PAC 93), Washington, DC, 17-20 May 1993.

[27] D. Schulte, *Study of Electromagnetic and Hadronic Background in the Interaction Region of TESLA.*, Ph.D. thesis, University of Hamburg 1996.

[28] N.Merminga, J.Irwin, R.Helm, R.D.Ruth, *Collimation Systems for a TEV Linear Collider*, SLAC Pub. 5165 Rev. (1994)

[29] I.Baishev, A.Drozhdin, N.Mokhov, *STRUCT Program User's Reference Manuel*, SSC-MAN-0034, February 1994.

[30] Handbook of Chemistry and Physics, Chemical Rubber Publishing Company (1976)

[31] K.L.F. Bane, P.L. Morton, *Deflection by the Image Current and Charges of a Beam Scraper*, SLAC Pub. 3983 (1986)

[32] Kaoru Yokoya, *Impedance of Slowly Tapered Structures*, CERN SL/90-88 (1988)

[33] A.Chao, *Physics of Collective Beam Instabilities in High Energy Accelerators*, J.Wiley & Sons, New York (1993)

[34] B. Rossi, *High-Energy Particles*, Prentice-Hall, New York, 1952.

[35] I.S. Baishev, M.A. Maslov, M. Seidel, *Design Study of a Beam Dump for the TESLA and S-Band Test Facilities at DESY*, DESY-TESLA-95-10, 1995.

[36] NLC-ZDR Design Group, *Zeroth Order Design Report for the Next Linear Collider*, SLAC, February 1996.

[37] K. Tesch, *A Note on Residual Radioactivity of Beam Absorbers for a Linear Collider*, DESY, March 1996.

[38] D.R. Walz, A. McFarlane, E. Lewandowski, *Beam Dumps, Stoppers and Faraday Cups at SLC*, SLAC-Pub. 4967, 1989.

[39] J. Kidd et al.,PAC IX, Washington, 1981.